Small strain shear stiffness anisotropy of a saturated clayey loess

Lu Zuo[a], Ling Xu[a,#], Béatrice Anne Baudet[b], Chongyang Gao[c], Chuang Huang[a]

[a]Department of Civil Engineering, School of Human Settlements and Civil Engineering, Xi'an Jiaotong University, Xi'an, China

[b]Department of Civil, Environmental and Geomatic Engineering, University College London, U.K.

[c]Architectural Engineering Institute, Northeast Electric Power University, Jilin, China

[#]corresponding author

Abstract

The mechanical behaviour of clayey loess is strongly affected by the soil structure, but although anisotropy has been identified in loess by some, the anisotropy of small strain behaviour is rarely reported. This paper presents an experimental study on the inherent and stress-induced small strain shear stiffness anisotropy of a clayey loess from China. Both undisturbed and reconstituted specimens were tested with bender elements under isotropic compression and shearing conditions. Under isotropic stress state, an inherent anisotropy was found for undisturbed specimens, while the reconstituted specimens prepared by moist tamping behaved isotropically. During shearing, the ratio of horizontal to vertical shear moduli of the undisturbed specimens decreased due to both an increase of stress anisotropy and the destruction of the intact structure. On the other hand, the stiffness ratio of the reconstituted specimens only decreased due to stress anisotropy and it became more anisotropic at the critical state. This study reveals the influence of intact structure and inherent anisotropy on the behaviour of loess soils, which cannot be reproduced by compaction, thus highlighting the importance of characterising the undisturbed loess.

Keywords

Loess, Laboratory testing, Anisotropy, Small strain stiffness, Soil structure

Introduction

Structured soils often display an anisotropic mechanical behaviour. In sands, during natural deposition or sample preparation, an orientated soil fabric tends to form because of gravity, resulting in an anisotropic mechanical behaviour (e.g. Arthur & Menzies, 1972; Bellotti et al., 1996; Ezaoui & Di Benedetto, 2009). Bahadori et al. (2008) reported that the initial anisotropy of sand decreases when there is a presence of silts, since the sand-sand particle contacts are interrupted and a more disturbed soil fabric is obtained. Similarly, Ghadr (2020) observed that the initial anisotropy is reduced when the sand is reinforced with a small amount of fibres. Anisotropic behaviour is also largely reported for clays (e.g. Jovičić & Coop, 1998; Callisto & Rampello, 2002; Gasparre et al., 2007a; Cho & Finno, 2010; Yimsiri & Soga, 2011). Gasparre et al. (2007a) presented the anisotropy of naturally deposited London Clay, which increases with depth, caused by a packed and orientated clay structure. Ignat et al. (2019) found that a soft post-glacial clay near Enköping, Sweden, shows anisotropic behaviour after cementation. It can be concluded that anisotropy is closely related to the development of soil structure.

The anisotropic behaviour of soils is generally investigated from two aspects: the inherent anisotropy, which results from the initial structural anisotropy of the soil; and the stress-induced anisotropy, which results from the further applied anisotropic stress conditions (Bellotti et al., 1996; Jiang et al., 1997; Jovičić & Coop, 1998; Fioravante, 2000, Mašín & Rott, 2014). There are different methods for the determination of soil anisotropy experimentally, for instance, testing different soil samples cored from vertical and horizontal directions (e.g. Xu et al., 2019), testing a single soil sample with the rotation of principal stress directions (e.g. Ignat et al., 2019), and testing the small strain stiffnesses of a single soil sample from different directions (e.g. Zuo & Baudet, 2020). Compared to the first two methods, in which there is uncertainty brought by non unique samples or the requirement for complex testing, the small strain stiffness measurement is a method that can avoid variability, by using a single sample. The stiffness being obtained at a strain level less than 10^{-3}%, can be considered as non-destructive to the soil structure during measurement (Viggiani & Atkinson, 1995b; Cai et al., 2015), while the small strain stiffnesses of a single soil sample from different directions can be obtained conveniently with a conventional triaxial apparatus equipped with bender elements, allowing the stiffness to be measured along a controlled stress path (Mitaritonna et al., 2014).

Bender element has been adopted in laboratory tests to measure the small strain shear stiffness in both vertical and horizontal planes (e.g. Viggiani & Atkinson, 1995b; Kuwano et al., 1999; Gasparre et al., 2007b; Ng & Yung, 2008; Choo et al., 2011; Li et al., 2012; Heitor et al., 2013; Mitaritonna et al., 2014). In the vertical plane, the small strain shear stiffnesses denoted as G_{vh} and G_{hv} are measured. G_{vh} is measured with a pair of vertically embedded bender elements, which transmit and receive shear waves propagating vertically and vibrating horizontally; G_{hv} is measured with a pair of horizontally embedded bender elements, which transmit and receive shear waves propagating horizontally and vibrating vertically. In the horizontal plane, the small strain shear stiffness G_{hh} is measured with a pair of horizontally embedded bender elements, which transmit and receive shear waves both propagating and vibrating horizontally. Based on the cross-anisotropic model, it is well established that the small strain shear stiffness G_{vh}, G_{hv} and G_{hh} is related to the soil structure, the void ratio, and the in-plane effective principal stresses (e.g. Jamiolkowski et al., 1995; Rampello et al., 1997; Santagata et al., 2005) with the expressions as:

$$\frac{G_{\mathrm{vh}}}{p_{\mathrm{r}}} = \frac{G_{\mathrm{hv}}}{p_{\mathrm{r}}} = S_{\mathrm{vh}}\, f(e)\left(\frac{\sigma'_{\mathrm{v}}}{p_{\mathrm{r}}}\right)^{n_{\mathrm{v}}}\left(\frac{\sigma'_{\mathrm{h}}}{p_{\mathrm{r}}}\right)^{n_{\mathrm{h}}} \tag{1}$$

$$\frac{G_{\mathrm{hh}}}{p_{\mathrm{r}}} = S_{\mathrm{hh}}\, f(e)\left(\frac{\sigma'_{\mathrm{h}}}{p_{\mathrm{r}}}\right)^{2n_{\mathrm{h}}} \tag{2}$$

where p_r is a reference stress, e is the void ratio, $f(e)$ is a function of void ratio with different proposed equations (e.g. Hardin & Richard, 1963; Pennington et al., 1997), S_{vh}, S_{hh}, n_v, and n_h are soil parameters (e.g. Viggiani & Atkinson, 1995; Jovičić & Coop, 1997) related to soil structure, such as particle arrangements and contacts (Cascante & Santamarina, 1996; Cho et al., 2006; Lee et al., 2007), σ'_v and σ'_h are effective principal stresses in vertical and horizontal direction respectively. To investigate the inherent anisotropy, small strain shear stiffness should be measured under isotropic stress condition (e.g. Jovičić & Coop, 1998; Teachavorasinskun & Lukkanaprasit, 2008; Ezaoui & Di Benedetto, 2009), then the equation (1) and (2) can be derived as:

$$\frac{G_{\mathrm{vh}}}{p_{\mathrm{r}}} = \frac{G_{\mathrm{hv}}}{p_{\mathrm{r}}} = S_{\mathrm{vh}} f(e) (\frac{p'}{p_{\mathrm{r}}})^{n_{\mathrm{v}}+n_{\mathrm{h}}} \quad (3)$$

$$\frac{G_{\mathrm{hh}}}{p_{\mathrm{r}}} = S_{\mathrm{hh}} f(e) (\frac{p'}{p_{\mathrm{r}}})^{2n_{\mathrm{h}}} \quad (4)$$

where p' is the mean effective stress. The small strain shear stiffness anisotropy is then expressed by the ratio of $G_{\mathrm{hh}}/G_{\mathrm{hv}}$.

Loess is a silt-sized Aeolian soil that is encountered all around the world (Li et al., 2016), with wide deposits in northwest China (Heller & Liu, 1982). Three different kinds of loess, namely sandy, silty, and clayey loess, can be classified based on the soil grading (Liu, 1985). It is well recognized that the mechanical behaviour of loess is strongly affected by its structure, especially for the clayey loess (Gao, 1988; Jiang et al., 2014; Xu & Coop, 2016; Ng et al., 2017a). However, the anisotropic behaviour of loess has rarely been reported, until recent years, and it is still less investigated. Liang et al. (2015) reported anisotropy in compressibility and shear strength (friction angle and cohesion) for a clayey loess by conducting simple laboratory tests such as direct shear test and unconsolidated undrained shear test. Xu et al. (2019) performed oedometer and triaxial tests on vertically and horizontally cored clayey loess under saturated conditions, and found anisotropy in the normal compression line (NCL) and critical state line (CSL) at relatively low stress levels, while both NCL and CSL became unique as the stress increased to higher levels. While there is evidence of anisotropy in loess behaviour, the small strain stiffness anisotropy is still missing in published literatures, although there has been research on the small strain behaviour of loess (Ng et al., 2017b; Song et al., 2017; Liu et al., 2019; Zuo et al., 2020). In this study, a triaxial shear apparatus equipped with both vertical and horizontal bender elements was used to determine the small strain shear stiffnesses G_{vh}, G_{hv} and G_{hh} of a typical clayey loess under different stress states. Both saturated undisturbed and reconstituted specimens were first isotropically compressed to different stress levels to investigate the inherent anisotropy, then followed by undrained or drained shearing to large strain level to achieve different stress ratios and the critical state, thus the induced anisotropy was allowed to be investigated at different stress and strain conditions. Scanning electron microscope (SEM) tests were conducted with specimens before and after shearing to investigate the micro-scale structure evolution. The inherent and stress-induced anisotropy in the small strain shear stiffness determined with bender element tests were analysed and the structure effect was discussed.

Materials, testing apparatus and procedures

Materials

The soils tested were recovered at a depth of 50m in a typical location of clayey loess deposition near Xi'an city, China. The structure was kept intact by using block sampling, each block sample was trimmed by hand and carefully sealed with layers of cling film and tape. It is an effective sampling method to keep the clayey loess structure intact as formerly reported by Xu & Coop (2016) and Xu et al. (2019).

Undisturbed specimens were vertically cored from the blocks with a cutting ring, while the soil's cut-offs were used to make reconstituted specimens. The soil has a clay content around 18%, silt content around 75%, and mean particle size D_{50} around 7.7μm. The intact void ratio varies in a narrow range within 0.72-0.74, the natural water content is around 15%, and the specific gravity is 2.74. The minerals of the clayey loess were determined by X-ray diffraction (XRD) and they consist mainly of quartz, albite, calcite, and clay minerals including illite, montmorillonite, and chlorite. More detailed soil properties can be referred to Xu & Coop (2016).

Testing apparatus and procedures

The tests were conducted in a triaxial system equipped with bender elements and local strain measuring LVDTs as illustrated in figure 1. The tested sample size was 50mm in diameter and 100mm in height. A pair of vertical bender elements was embedded in the top cap and pedestal to measure G_{vh} (figure 1, part 10), and a pair of horizontal bender elements was mounted on the side of the specimen (e.g. Pennington et al., 1997; Gasparre & Coop, 2006) to measure G_{hv} and G_{hh} (figure 1, part 11). A signal generator with a maximum applied voltage of 12V and an oscilloscope were used to generate and receive the signals respectively. The time-domain method, more specifically the first arrival method was used to determine the small strain stiffness. The time delay between transmitter and receiver elements was calibrated by "tip to tip" method. To minimize the uncertainty brought by near-field effects, a series of sinusoidal input signals of frequencies in the range 2-15kHz was used, and a common travel time was obtained by comparing all the received signals (e.g. Viggiani & Atkinson, 1995a; Jovičić et al., 1996; Viana da Fonseca et al., 2009). Two LVDTs for local axial strain measurement were directly glued on the specimen membrane (figure 1, part 12-14), and a system recommended by Ackerley et al. (2016) was set up for the local radial strain measurement, particularly on the horizontal wave propagation plane for travel length measurement (figure 1, part 3-7). The measuring range of the LVDTs was 0−10mm and the resolution was ±0.0004mm. Before tests, the triaxial cell, loading frames, and pressure controllers were all confirmed to be working normally, and the transducers, including load cell, water pressure transducer, and LVDTs were all calibrated. The L-shaped component with local LVDT (figure 1, part 5-7) for radial strain measurement was also calibrated with a micrometer to obtain the factor between the readings and true displacements.

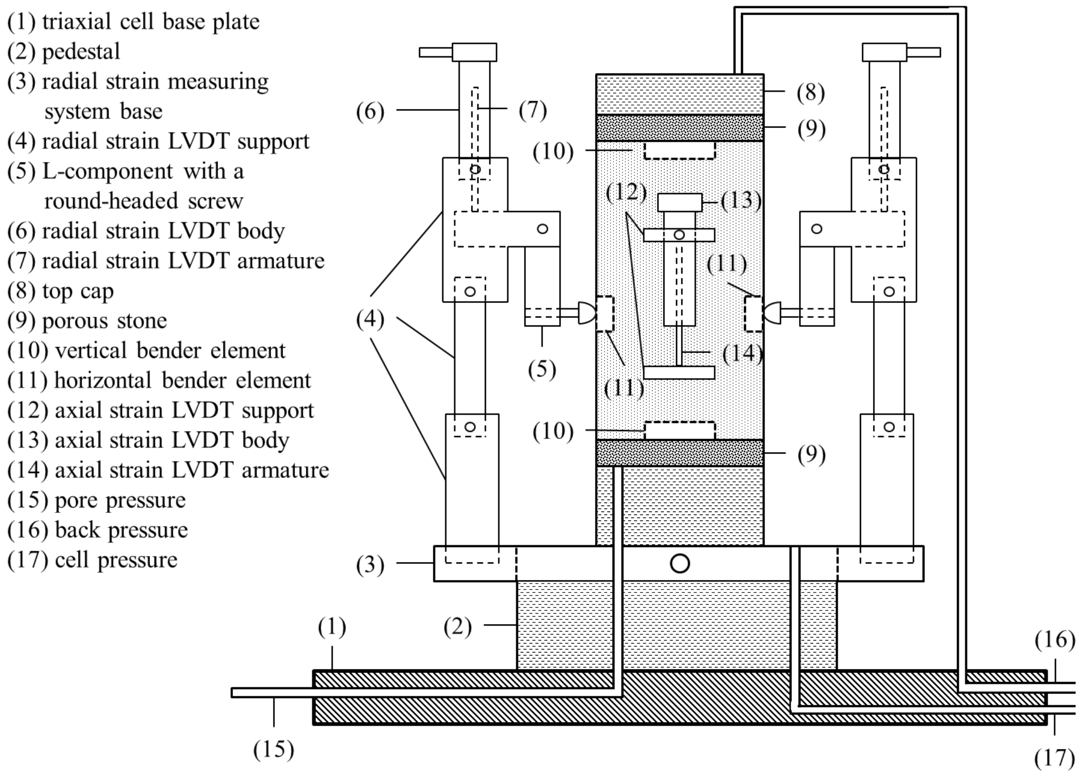

Figure 1 Schematic diagram triaxial apparatus equipped with vertical and horizontal bender elements and axial and radial LVDTs

Both undisturbed and reconstituted specimens were tested. For undisturbed specimens, a cutting ring with a chosen dimension was placed on the soil block and some downward pressure was applied, then the soil out of the ring edge was cut off by hand carefully to avoid any micro-cracks or structure destruction and the specimen was trimmed into the ring gradually (Xu & Coop, 2016). For reconstituted specimens, the moist tamping method was used for sample preparation. As compared to the slurry method, which is another commonly used sample preparation method, moist tamping method tends to create a soil structure more different to that of the in-situ samples (Li & Coop, 2019). The soil was first oven-dried and grinded to aggregate sizes less than

0.3mm to remove the existence of intact structure as much as possible. Then the soil was weighed according to the designed initial void ratio for the experiments (loose, medium-dense and dense) and mixed well at an initial water content of 7.5%, until a homogeneous fabric was obtained. Then the soil was compacted on the pedestal in 4 even layers with the help of a split mould. Each layer had a thickness of 25mm.

A modified membrane with a pair of lateral supporting parts was used, and after the specimens were set up in the triaxial system, horizontal bender elements were inserted and sealed with O-rings and latex rubber. After de-aired water flushing, the specimen was subjected to back pressure saturation to achieve a B-value above 0.95. After saturation, the cell pressure was increased in steps to conduct isotropic compression together with the bender element tests, and the maximum effective stress achieved was 600kPa. After compression, the specimens were sheared undrained or drained to reach the critical state, with the largest axial strain equal to 25%. The strain rate was 0.002%/min, which was slow enough for the full dissipation or the reliable measurement of the excess pore water pressure during shearing.

Typical stress-strain curves and stress paths are shown in figure 2. Figure 2(a) summarizes the paths in the v-lnp' plane, where v is the specific volume, along with the CSLs of both intact and reconstituted specimens. The undisturbed specimens were sheared from similar initial void ratio e_0 and initial mean effective stress p'_0 while the reconstituted specimens started from different states, the specimen tested undrained located much closer to the CSL than that sheared drained, indicating an initial denser state. From the shearing results presented in figure 2(b), both undisturbed specimens show a similar stiff behaviour, attributed to a strong intact structure effect that was also reported by Xu & Coop (2016). The denser initial state of the reconstituted specimen tested undrained compared to that tested drained is reflected in its much stiffer response (Fig. 2(c)). From figure 2(a) it is also noted that the reconstituted specimen sheared undrained started from a closer distance to its CSL than the intact undrained specimen, which may explain its high stiffness in spite of being reconstituted, and the strain softening as seen from the development of excess pore water pressure (Fig. 2(d)).

During shearing, the bender element tests were conducted at stress ratio η of 0.2, 0.4, 0.6, 0.8, 1.0, and 1.2 as illustrated in figure 2(e), where η is calculated as q/p' and q is the deviatoric stress. The triaxial loading was not stopped when the bender element signals were captured, since the shearing strain rate was slow enough to obtain stable received signals. The stress ratio at critical state is 1.25 as shown in figure 2, which means there is little variation of η value after reaching 1.2 as the axial strain keeps increasing. However, this strain development may also cause the anisotropy evolution, so more bender element tests were conducted at different axial strain levels as the specimens approaching the critical state.

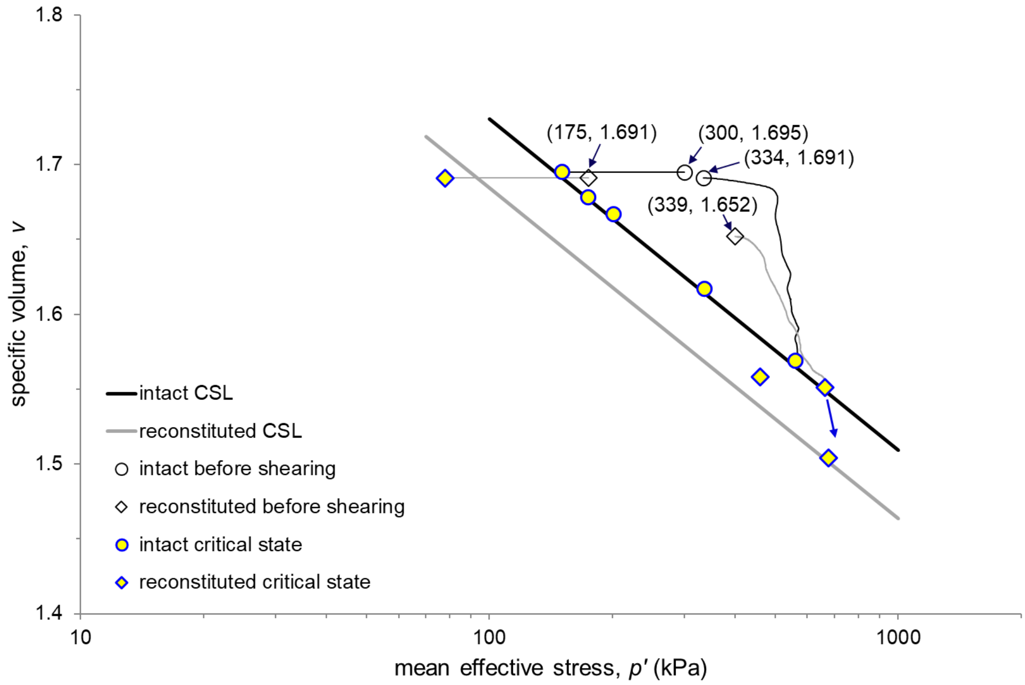

1.8
1.7
1.6
1.5
1.4
specific volume, v
10
100
1000
mean effective stress, p′ (kPa)
(175, 1.691)
(300, 1.695)
(334, 1.691)
(339, 1.652)
intact CSL
reconstituted CSL
intact before shearing
reconstituted before shearing
intact critical state
reconstituted critical state

2(a)

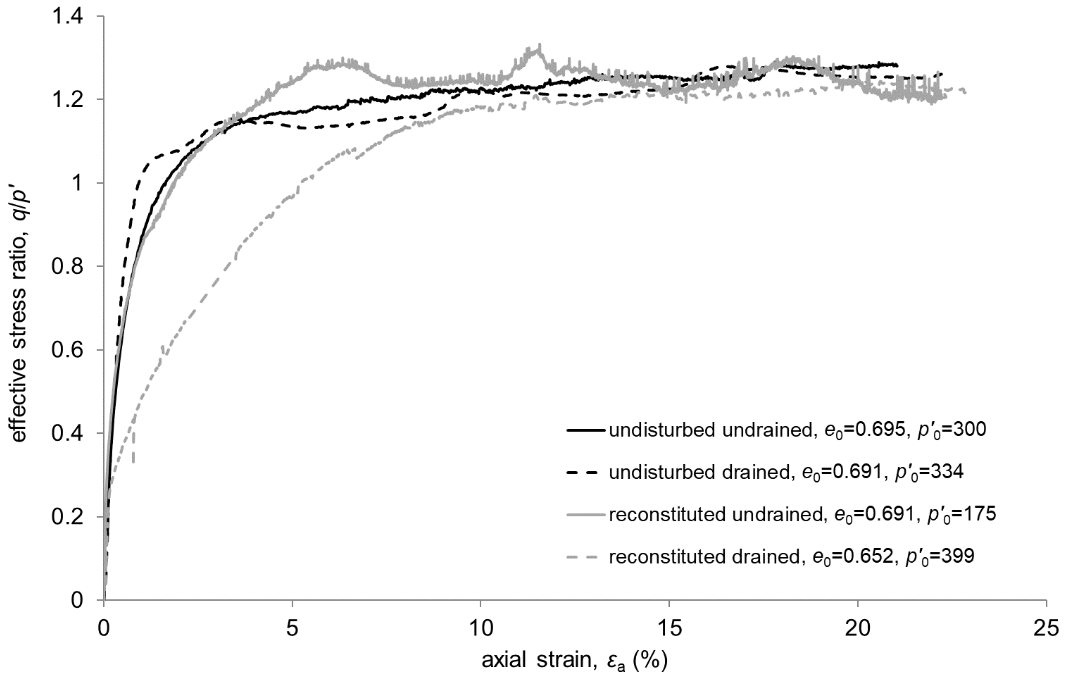

1.4
1.2
1
0.8
0.6
0.4
0.2
0
effective stress ratio, q/p′
0
5
10
15
20
25
axial strain, εa (%)
undisturbed undrained, e0=0.695, p′0=300
undisturbed drained, e0=0.691, p′0=334
reconstituted undrained, e0=0.691, p′0=175
reconstituted drained, e0=0.652, p′0=399

2(b)

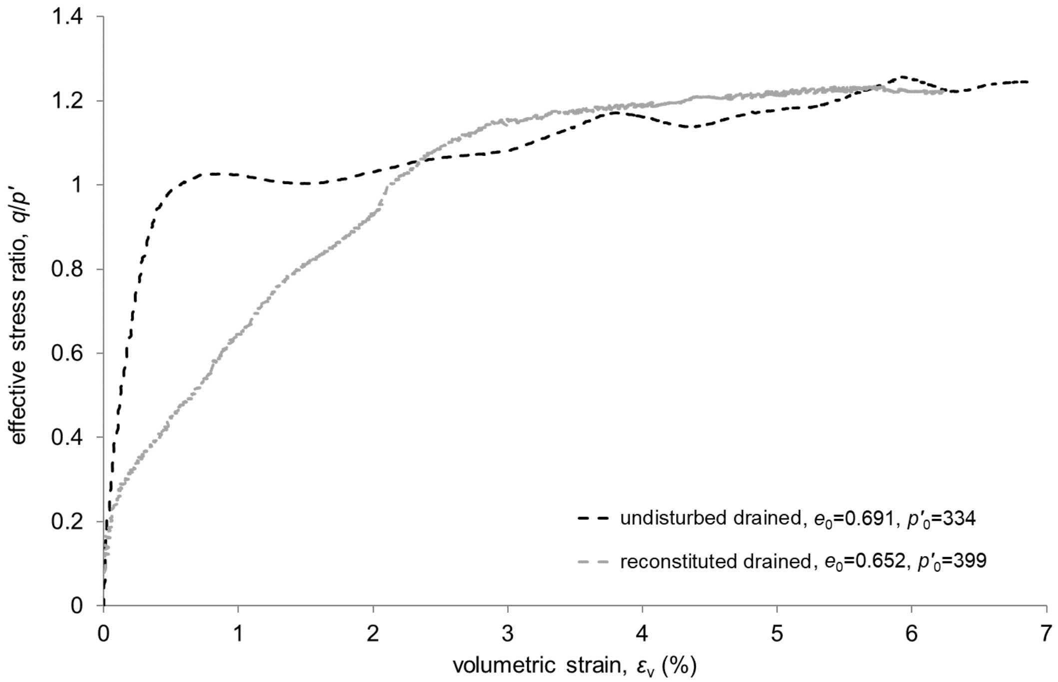
effective stress ratio, q/p′
volumetric strain, εv (%)
undisturbed drained, e0=0.691, p′0=334
reconstituted drained, e0=0.652, p′0=399
0
0.2
0.4
0.6
0.8
1
1.2
1.4
0
1
2
3
4
5
6
7

2(c)

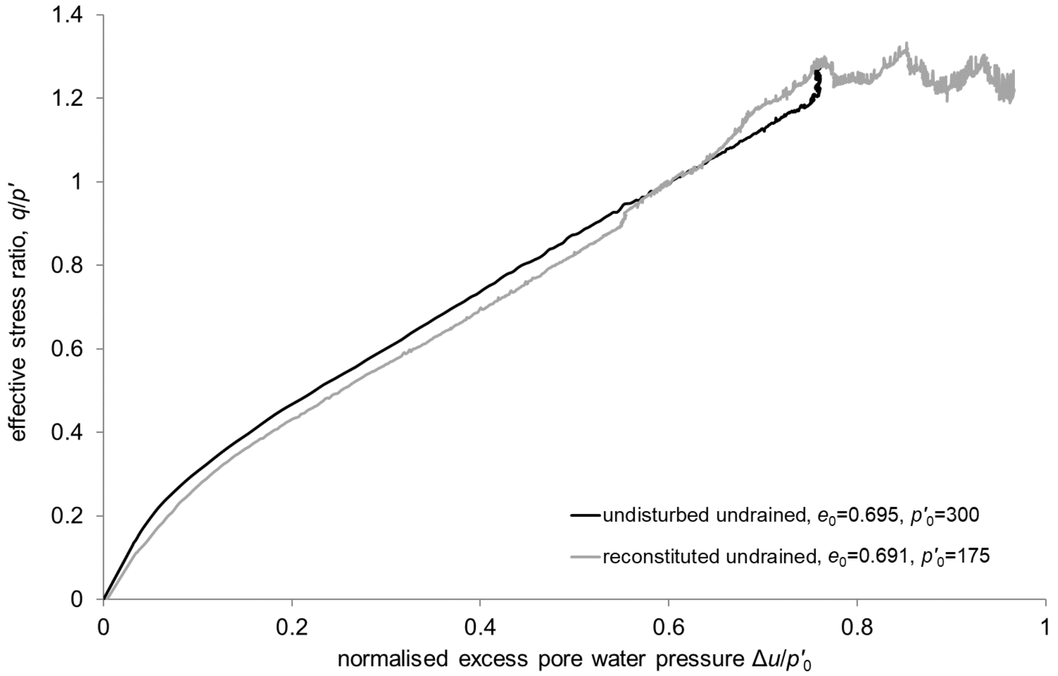
effective stress ratio, q/p′
normalised excess pore water pressure Δu/p′0
undisturbed undrained, e0=0.695, p′0=300
reconstituted undrained, e0=0.691, p′0=175
0
0.2
0.4
0.6
0.8
1
1.2
1.4
0
0.2
0.4
0.6
0.8
1

2(d)

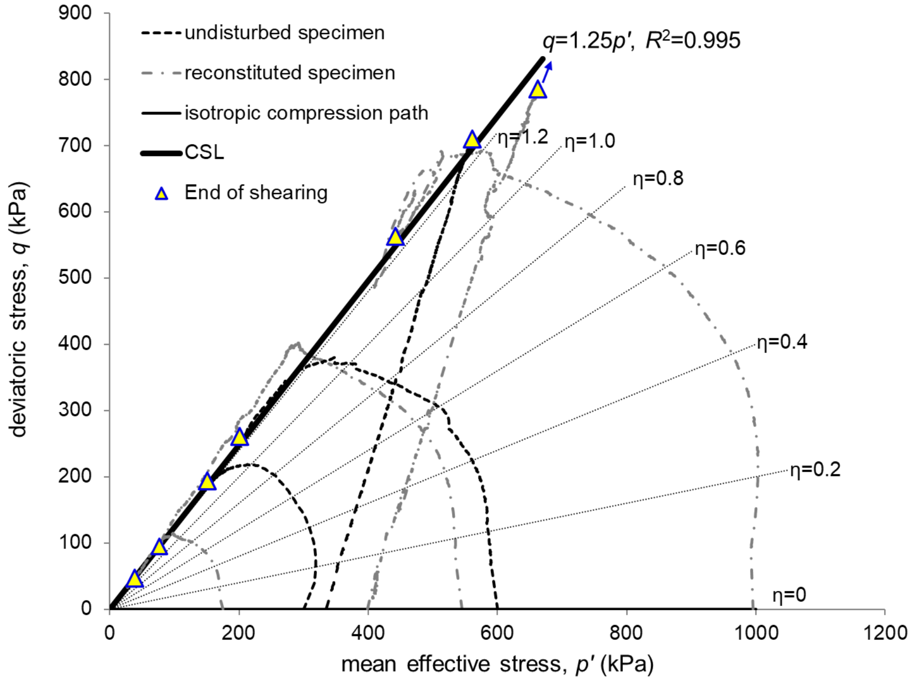

2(e)

Figure 2 Typical results (a) CSLs and shear paths in *v*-ln*p'* plane (b) shearing stress-strain curves (c) effective stress ratio vs. volumetric strain in drained tests (d) effective stress ratio vs. excess pore water pressure in undrained tests (d) CSLs and shear paths in *v*-ln*p'* plane (e) compression and shearing stress paths and stress ratios where small strain shear stiffness measured

Inherent anisotropy

Isotropic compression

The isotropic compression curves obtained for both undisturbed and reconstituted specimens are plotted in figure 3 in terms of specific volume *v* against mean effective stress *p'*. It shows that a unique NCL can be reached for undisturbed specimens at *p'* around 600kPa, which is in good agreement with the results reported by Xu & Coop (2016), indicating a good specimen quality as well. For reconstituted specimens looser or denser than the undisturbed ones, the compression curves tend to converge to a unique intrinsic compression line (ICL). The compression curves of undisturbed specimens all reach the state well outside the ICL, indicating a clear structure effect. Note that the undisturbed specimens do not yield to the NCL before 600kPa, which means the intact structure does not suffer distinct damage during compression.

With the measurements of local LVDTs, the axial and radial deformations during compression can be determined. The axial strain ε_a was calculated as the average value of the axial strains determined by the two axial local LVDTs, and the sum of the radial deformations determined by the two radial local LVDTs was used to calculate the radial strain ε_r. It allows an analysis of inherent anisotropy from a global strain point of view. Figure 4 shows the strain increment ratio of $\Delta\varepsilon_r/\Delta\varepsilon_a$ during compression, where $\Delta\varepsilon_r$ and $\Delta\varepsilon_a$ are the increments of radial and axial strain in each compression stress level, comprising both elastic and plastic components. It shows that despite a little scattered, the ratio for the undisturbed specimen remains around 1.98 during compression, indicating an anisotropic behaviour. The ratio for the reconstituted specimen is around 1.00, showing a more isotropic behaviour. Similar phenomenon is also reported by Jovičić & Coop (1998) for London clay.

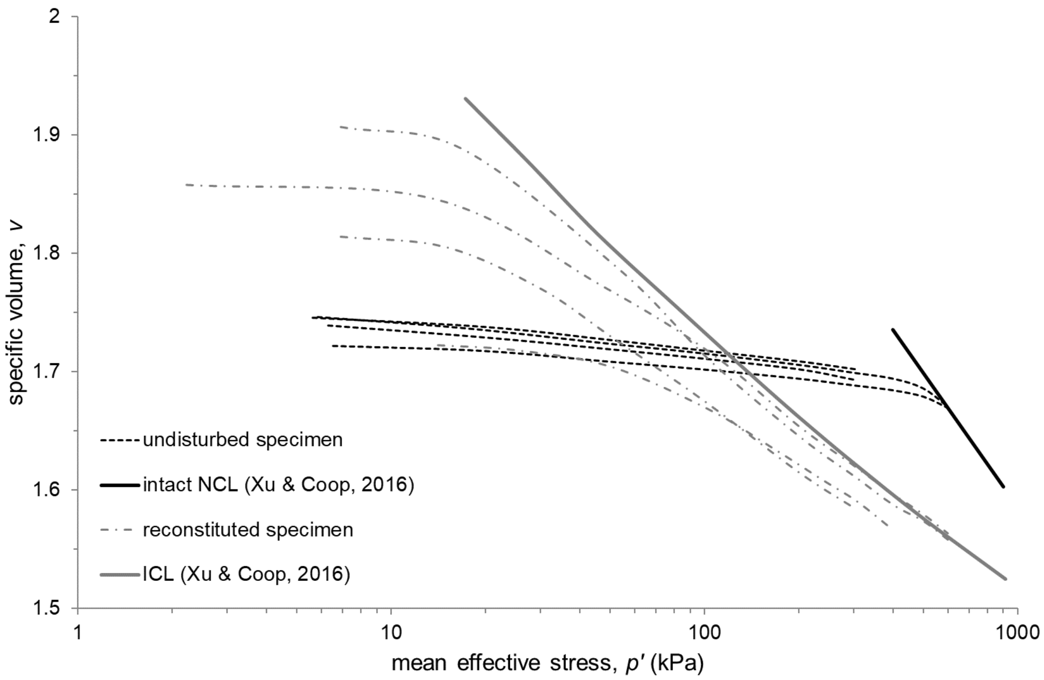

Figure 3 Isotropic compression curves of undisturbed and reconstituted specimens

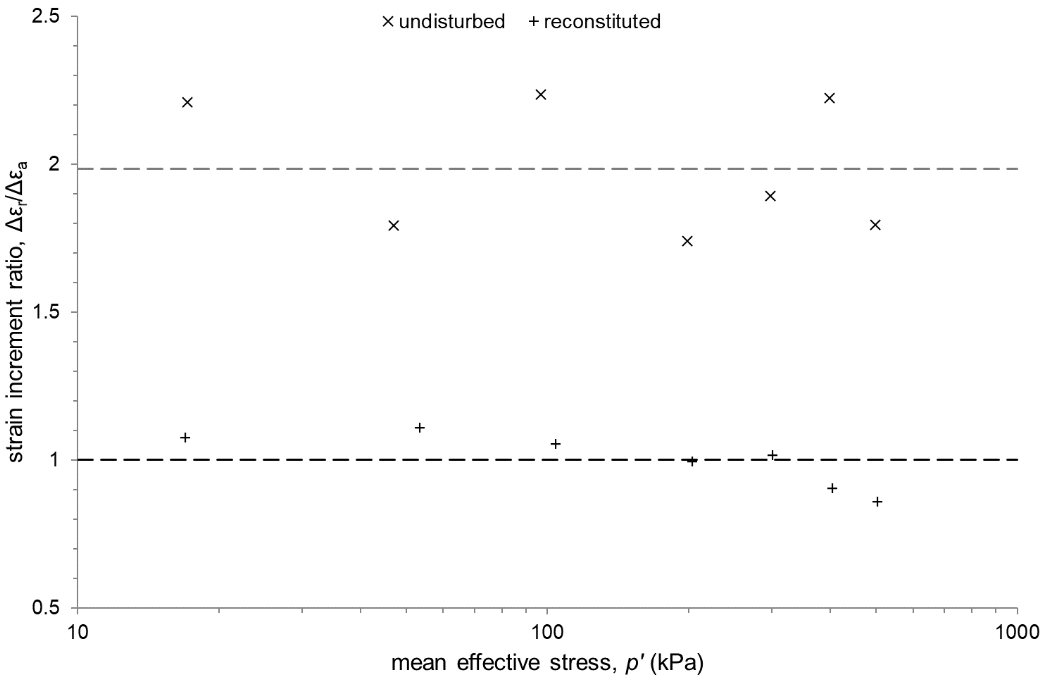

Figure 4 Strain increment ratio of undisturbed and reconstituted specimens during isotropic compression

Small strain shear stiffness during isotropic compression

The small strain shear stiffness data points obtained for undisturbed specimens during compression are plotted in figure 5(a), and the stiffness ratios of G_{vh}/G_{hv} and G_{hh}/G_{hv} are plotted in figure 5(b), both against *p'*. It has been proved that when a unique normal compression line is reached, the small strain shear stiffness is only related to the stress condition and a unique NCL in the $\ln G_0$-$\ln p'$ plane can be found (e.g. Jovičić & Coop, 1997; Zuo & Baudet, 2020). However, as shown in figure 3, most of the small strain stiffness data points measured during compression were under low stress levels and still far from reaching the NCL, which means the effect of void ratio should be taken into consideration. In figure 5, the stiffness value is then normalized by the void ratio function $f(e)=e^{-1.3}$, which has been commonly used for fine-grained soils (e.g. Jamiolkowski et al., 1995; Pennington et al., 1997; Li et al., 2012), to remove the influence of void ratio. It can be observed that the values of G_{vh} are slightly higher than those of G_{hv} with an average stiffness ratio of 1.02, which is consistent with the cross-anisotropy model. The values of G_{hh} are higher than those of the other two, and the value of stiffness anisotropy ratio G_{hh}/G_{hv} generally lies in the range of 1.2 to 1.35 with an average value of 1.27, indicating an inherent anisotropy degree similar to some natural clays (e.g. Callisto & Rampello, 2002; Teachavorasinskun & Lukkanaprasit, 2008; Kim & Finno, 2012; Li et al., 2012). Like for the global strains shown earlier in figure 4, the test data indicate cross-anisotropy although a direct comparison cannot be made. According to equation (3) and (4), straight lines can be fitted for the stiffness data points in a double logarithmic graph.

The fitting lines are shown in figure 5(a) together with the expressions, and the reference stress p_r is taken as 1kPa. It shows that the fitting results are quite good and the two lines are parallel to each other, indicating a same value of n_v and n_h, which equals to 0.227 (half of 0.454).

Xu et al. (2019) performed oedometer and triaxial experiments on undisturbed specimens cored vertically and horizontally from the same sample of clayey loess tested here, which was retrieved as described earlier. The results of one-dimensional compression show that the yielding stress of the vertically cored specimen is 1.24 times as large as that of the horizontally cored specimen. Similarly, the results of undrained shearing show that under the same initial confining pressure, the deviatoric stress of vertically cored specimens increases faster than that of horizontally cored specimens, and the peak strength of vertically cored specimens is averagely 1.55 times as large as that of the horizontally cored specimens. It then can be concluded that the soil inherent anisotropy determined from small strain shear stiffness measurements can be used as an indicator of anisotropic mechanical behaviour at different stress-strain conditions.

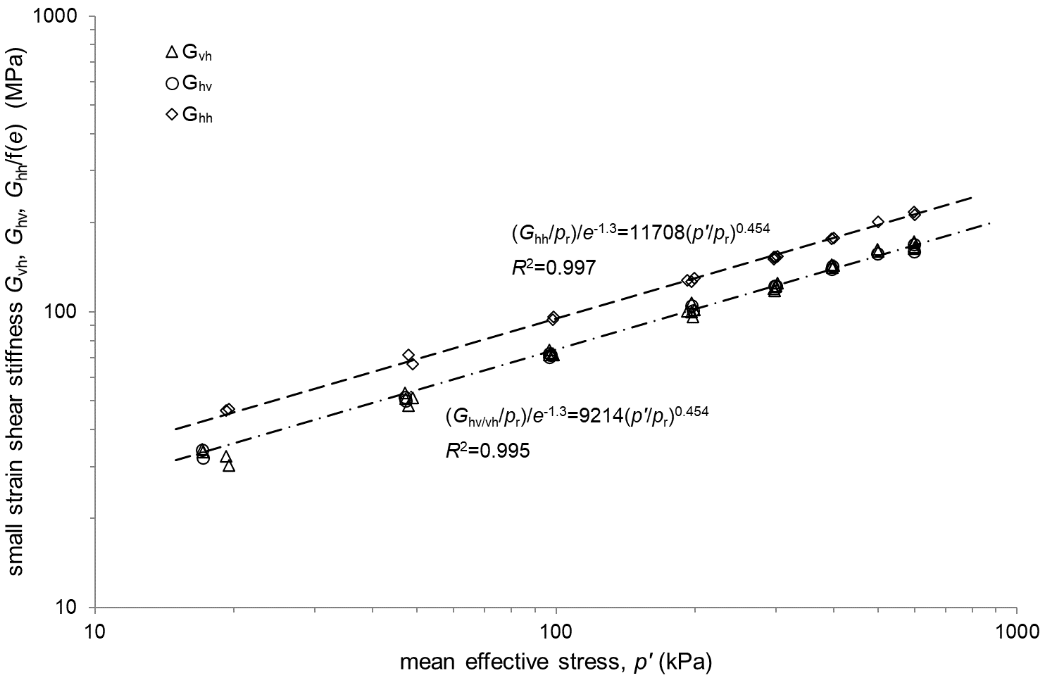

5(a)

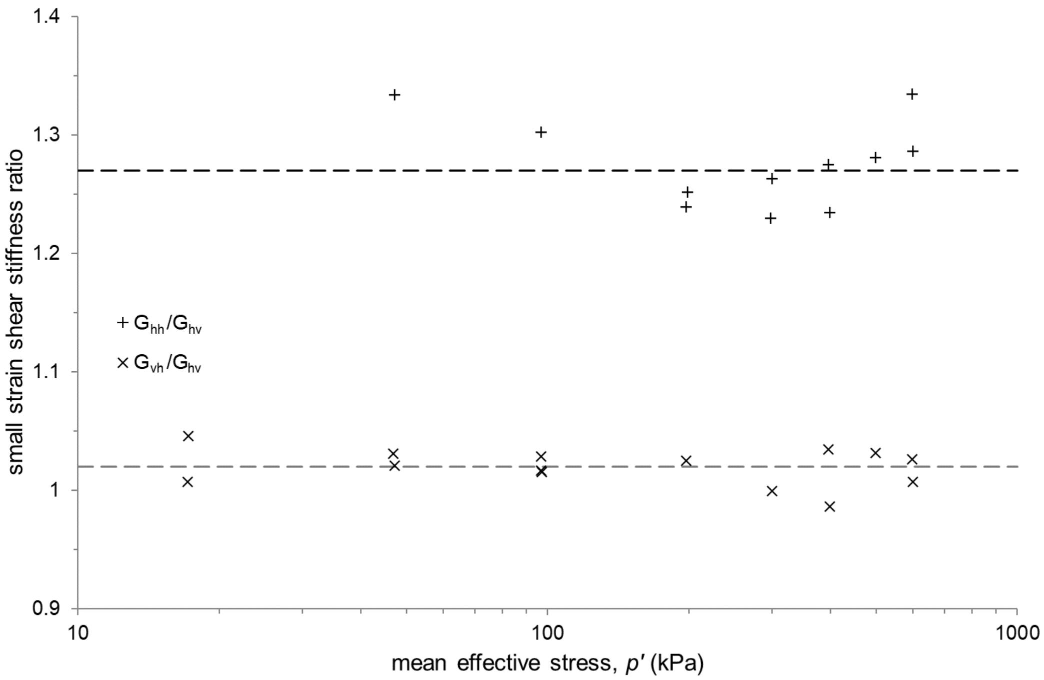

5(b)

Figure 5 Small strain shear stiffness for undisturbed specimens under isotropic stress condition (a) stiffness in vertical and horizontal planes (b) stiffness ratios

Similarly, the small strain shear stiffness results of reconstituted specimens under isotropic compression are shown in figure 6. It shows that the inherent anisotropy is much reduced due to the destruction of the intact structure during specimen preparation. As shown in figure 6(b), the stiffness anisotropy ratio G_{hh}/G_{hv} mainly ranges between 0.96 and 1.03 with an average value of 1.01, and the ratio G_{vh}/G_{hv} mainly ranges between 0.96 and 1.00 with an average value of 0.98. The scatter in data points is possibly due to the complexity and subjectivity of the determination of arrival time, and the high sensitivity of the stiffness ratio to the arrival time as well. As shown in figure 6(b), a decrease of only 2 microseconds in the arrival time of G_{hh} (which is also a reasonable result from the signal analysis) makes the stiffness anisotropy ratio G_{hh}/G_{hv} increase from 0.96 (solid red circle) to 1.00 (dotted red circle). Although there are some uncertainties brought by the limitation of testing method, it still clearly indicates an isotropic behaviour, which is in good agreement with the global strain increment ratio as shown in figure 4. Based on the data points with effective stress in excess of 300kPa, the NCL in the lnG_0-lnp' plane can be determined as shown in figure 6(a). There are some data points above the NCL under lower stresses since they are too far away from reaching the ICL in the v-lnp' plane and the effect of void ratio cannot be fully normalized. This phenomenon seems independent with the testing method, since Yang & Liu (2016) found similar results when measuring the small strain shear stiffness of sand-fines mixtures using both bender element and resonant column techniques. It shows that compared to undisturbed specimens, reconstituted specimens have much lower S_{vh} and S_{hh} value of

2599, and higher n_v and n_h values of 0.321 (half of 0.642), indicating a much less stable soil structure (Cascante & Santamarina, 1996; Lee et al., 2007; Yang & Liu, 2016), which is consistent with the compression behaviour.

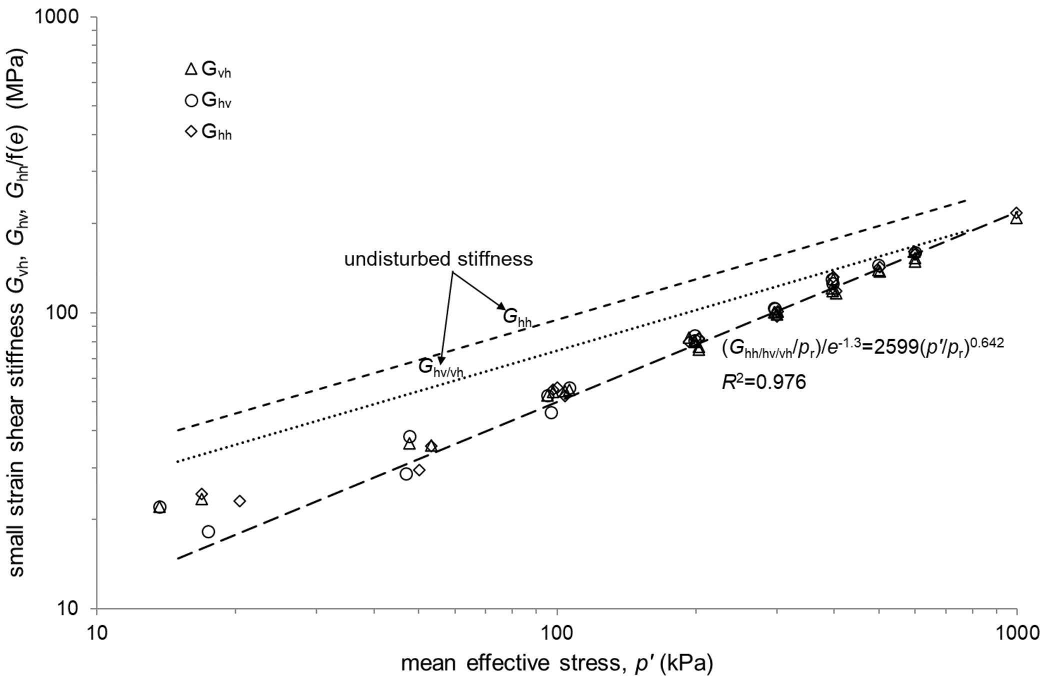

6(a)

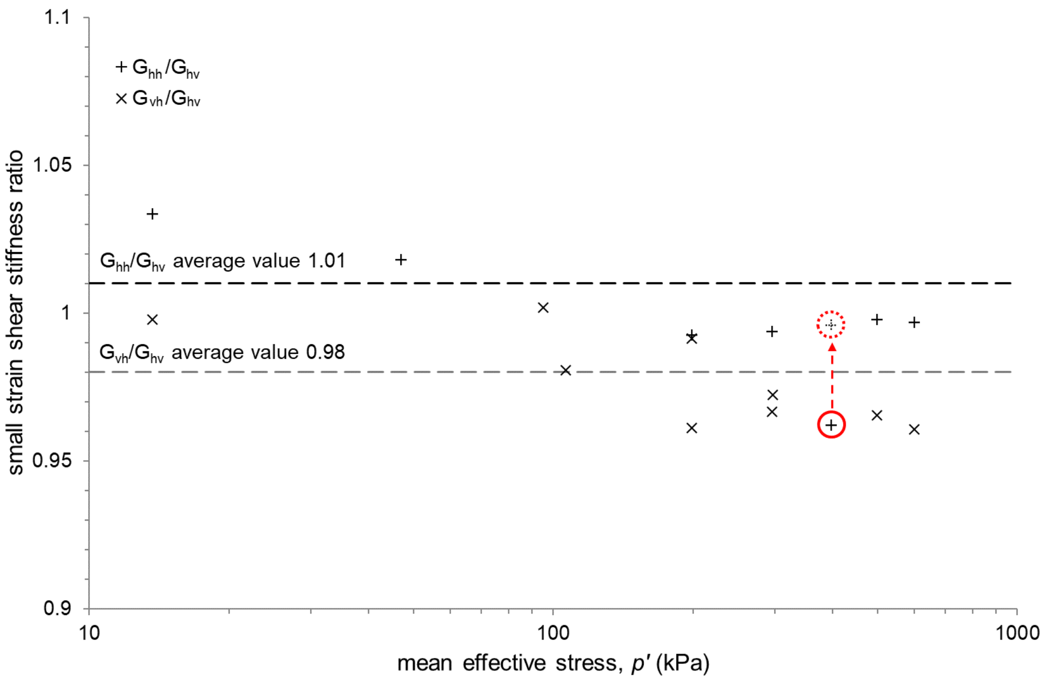

6(b)

Figure 6 Small strain shear stiffness for reconstituted specimens under isotropic stress condition (a) stiffness in vertical and horizontal planes (b) stiffness ratios

SEM observations

Both horizontal and vertical original planes of undisturbed and reconstituted specimens before compression were set to SEM tests, and the representative results are shown in figure 7 and 8 respectively. For undisturbed loess, it can be observed in figure 7 that silty particles are well coated and combined by clay minerals to form large aggregates, and the aggregates are again well bonded at the contacts by clays with some large pores in between. It is interesting to notice that the aggregates tend to show a platy shape, with their main surfaces on the horizontal plane, while on the vertical plane, more surfaces with elongated shape can be observed. It indicates that during deposition, the long axes of aggregates preferred to lie horizontally under gravitational force, and this orientated aggregates/particles arrangement results in an inherent anisotropy. What has been found here is supported by the researches of clays and discrete element method (DEM) simulations (e.g. Mitaritonna et al., 2014; Wang & Mok, 2008). For reconstituted loess, a quite different soil structure can be observed clearly as shown in figure 8. Compared to undisturbed loess, large aggregates were destroyed during remolding, there are more single silty particles with much less coated surfaces, and instead of aggregates coatings and bondings, the clay particles are more like to form clay aggregates themselves. Thus, the particle contacts are less strengthened, resulting in a much weaker structure and further much lower small strain stiffness. On both horizontal and vertical plane, the particles appear to be randomly orientated, which is more likely to result in an isotropic inherent behaviour.

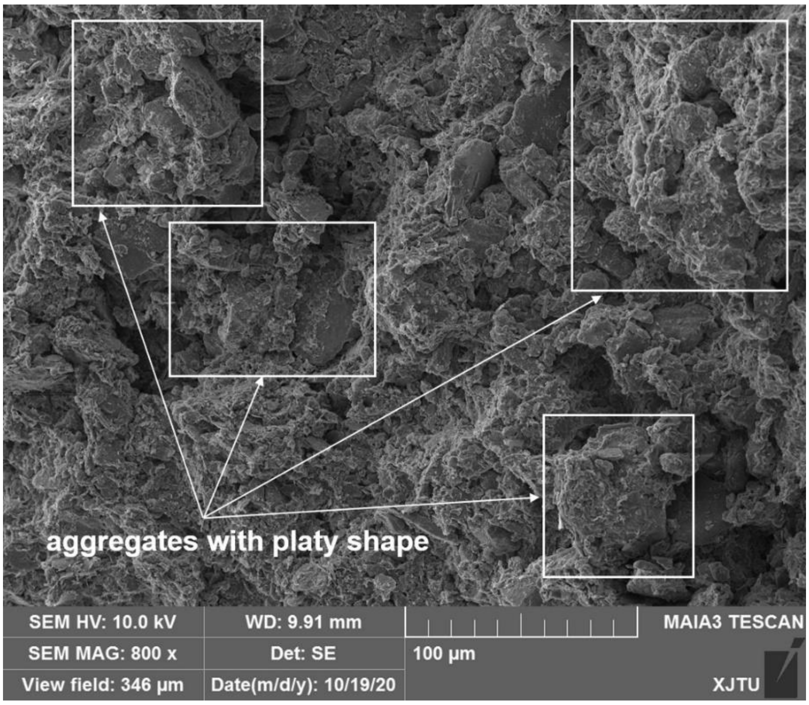

7(a)

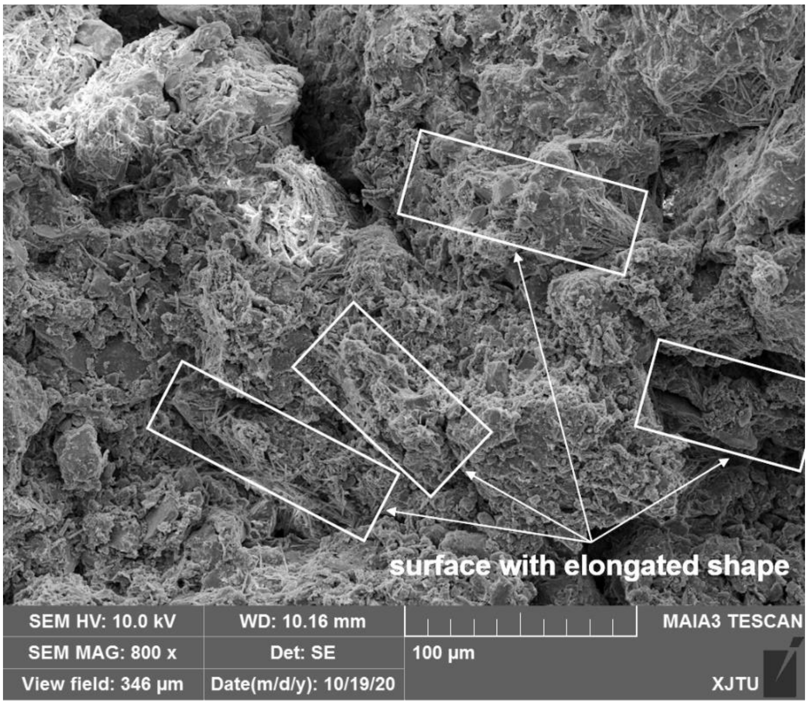

7(b)

Figure 7 SEM observations of undisturbed loess before compression (a) horizontal plane (b) vertical plane

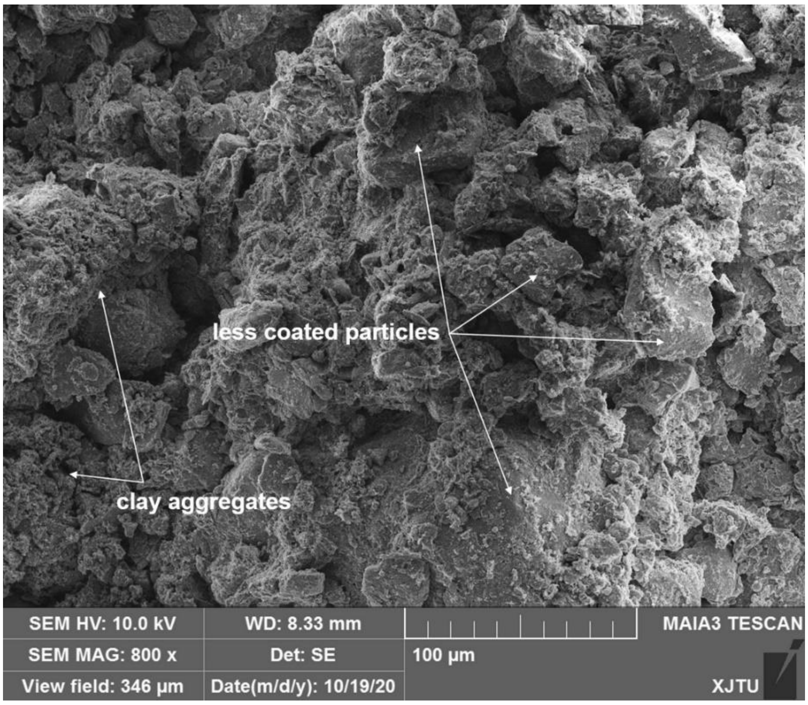

8(a)

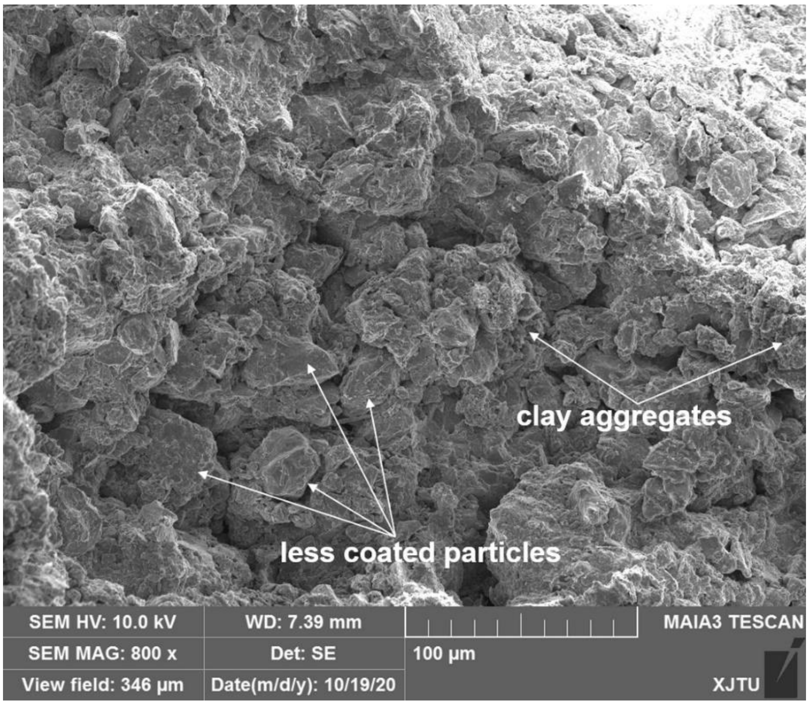

8(b)

Figure 8 SEM observations of reconstituted loess before compression (a) horizontal plane (b) vertical plane

Stress-induced anisotropy

After isotropic consolidation, the loess specimens were set to triaxial shearing. As shown by the stress-strain curves in figure 2(a), the specimens first experienced a quick stress ratio increment without much strain development, especially for the undrained sheared ones. Afterwards, the axial strains of the specimens increased much further to reach the critical state with little change in the stress ratio. The evolution of small strain stiffness anisotropy during shearing was studied based on these two stages.

Stage I-Anisotropy at different stress ratios

The stiffnesses measured with bender elements for undisturbed specimens at different stress ratios are plotted in figure 9, together with the NCLs obtained from isotropic stress condition. In order to eliminate the influence of strain development as much as possible, only the data points with corresponding axial strains less than 2% were selected for undisturbed specimens. It shows in figure 9(a) that when plotted against p', as η increases, there is no obvious stiffness reduction observed for G_{vh} and G_{hv}, and the $G_{vh/hv}$ NCL still fits the data points well even when the value of η is large; on the other hand, G_{hh} falls below the G_{hh} NCL immediately, and when η reaches 1.2, G_{hh} is reduced by about 23% and becomes almost the same with $G_{vh/hv}$, and the ratio G_{hh}/G_{hv} decreases from 1.27 to 0.98. Thus, the overall trend can be concluded as the stiffness anisotropy keeps decreasing for undisturbed loess at this stage. Considering equation (1) and (2), when $G_{hh/vh/hv}$ is plotted against p' at anisotropic stress state, it cannot tell whether the development of anisotropy is simply due to the increase in σ'_v (i.e. increase in stress anisotropy), or the soil structure evolution also makes a contribution. Then the stiffnesses are plotted against the product of effective principal stresses as shown in figure 9(b), specifically, $\sigma'_v \cdot \sigma'_h$ for G_{vh} and G_{hv}, and $\sigma'_h \cdot \sigma'_h$ for G_{hh}. It shows that all data points are still on the NCLs and do not fall below the lines even at η equals to 1.2. It indicates that the decrease in anisotropy is induced only by the stress anisotropy, while the soil structure does not suffer distinct damage at this stage.

Meanwhile at the beginning of shearing, with the measurement of local LVDTs, the initial increment of shear strain $\Delta\varepsilon_s$ can be calculated as:

$$\Delta\varepsilon_{\mathrm{s}} = \frac{2}{3}(\Delta\varepsilon_{\mathrm{a}} - \Delta\varepsilon_{\mathrm{r}}) \tag{5}$$

Then the initial shear stiffness G_0 can be calculated as:

$$G_0 = \frac{1}{3}\frac{\Delta q}{\Delta\varepsilon_{\mathrm{s}}} \tag{6}$$

where Δq is the increment of deviatoric stress measured by the load cell. It can be observed in figure 9(a) that for undisturbed specimens, the calculated G_0 data points plot lower than the NCL of $G_{vh/hv}$ determined with bender elements, and can be fitted with a line parallel to the NCL with some scatter. It has been reported that a shear strain level less than 10^{-4}% can be maintained in bender element test (Pennington et al., 2001; Leong et al., 2005). However, the shear strain level, at which G_0 is calculated in this study, is generally 10^{-3}%, which may explain the lower G_0 values. Furthermore, the disturbance to the specimen during docking period makes it difficult to control the accuracy of initial shear strain, resulting in more scattered results.

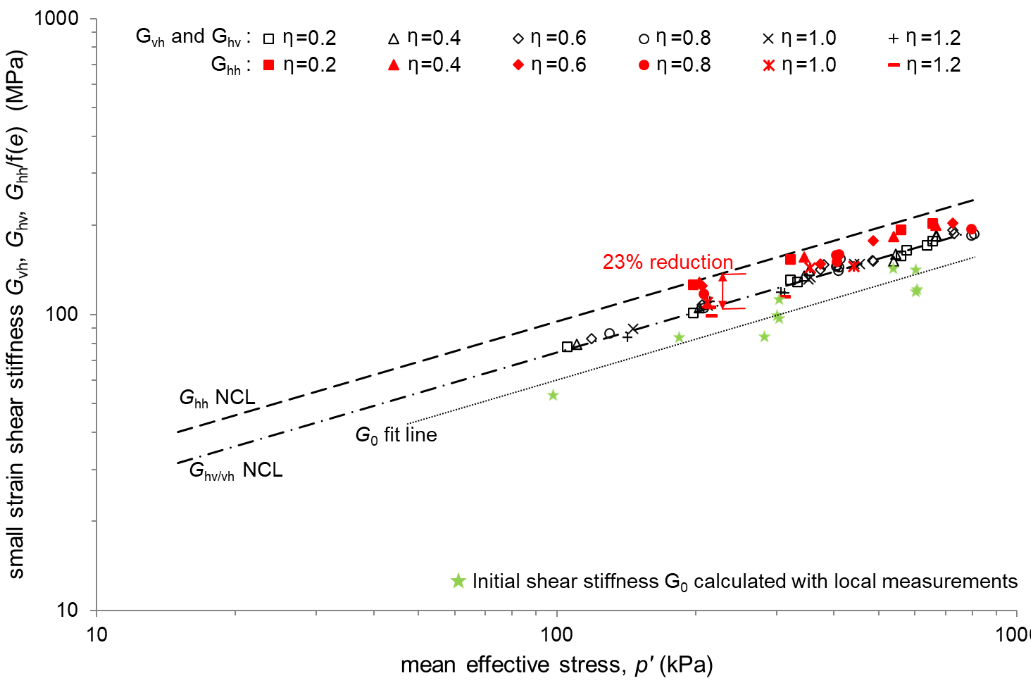

9(a)

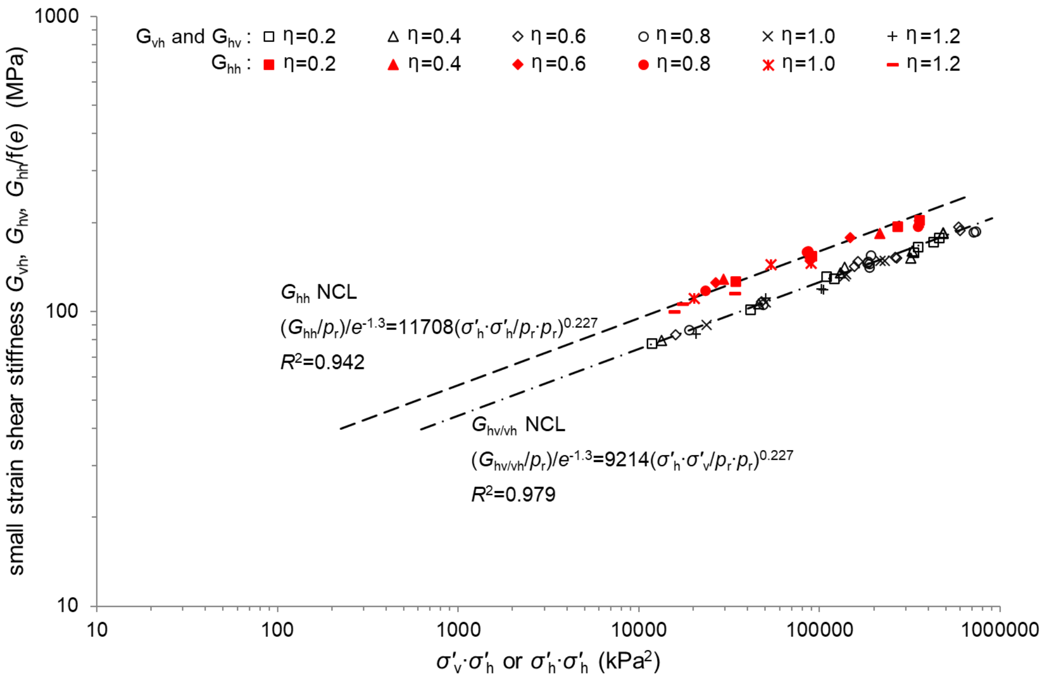

9(b)

Figure 9 Small strain shear stiffness of undisturbed specimens at different stress ratios (a) against the mean effective stress (b) against the product of effective principal stresses

The small strain shear stiffnesses of reconstituted specimens measured with bender elements at different stress ratios are shown in figure 10. In this case, only the data points with corresponding axial strains less than 5% were selected. Similar to the results of undisturbed ones, it can be observed that when plotted against *p'* in figure 10(a), G_{vh} and G_{hv} are still on the NCL while G_{hh} keeps decreasing as the stress ratio increases, and when η reaches 1.2, G_{hh} is reduced by about 25% and the average value of stiffness ratio G_{hh}/G_{hv} is around 0.75. Considering the initial isotropic behaviour, it can be concluded that the reconstituted specimens become more anisotropic as the stress ratio increases. When plotted against the product of effective principal stresses in figure 10(b), all stiffnesses are on the NCL and there is no significant variation even the stress ratio is high. It can be revealed that the development of anisotropy of reconstituted specimens within this stage is mostly induced solely by the anisotropic stress state. For the calculated initial shear stiffness G_0, it again shows lower values comparing to $G_{hh/hv/vh}$ due to the larger shear strain level as shown in figure 10(a).

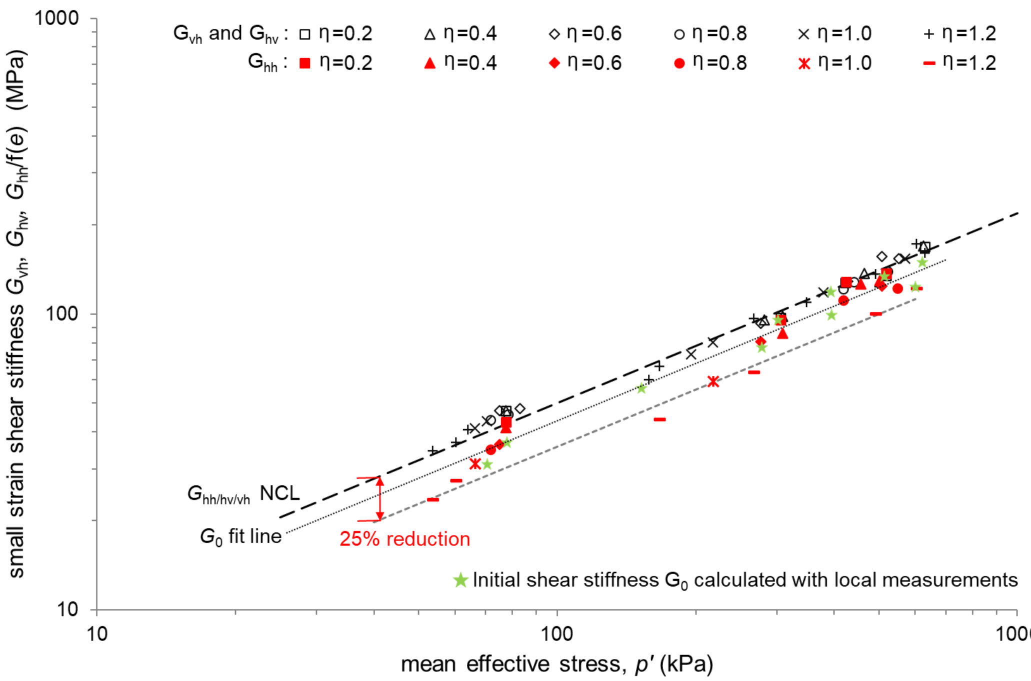

10(a)

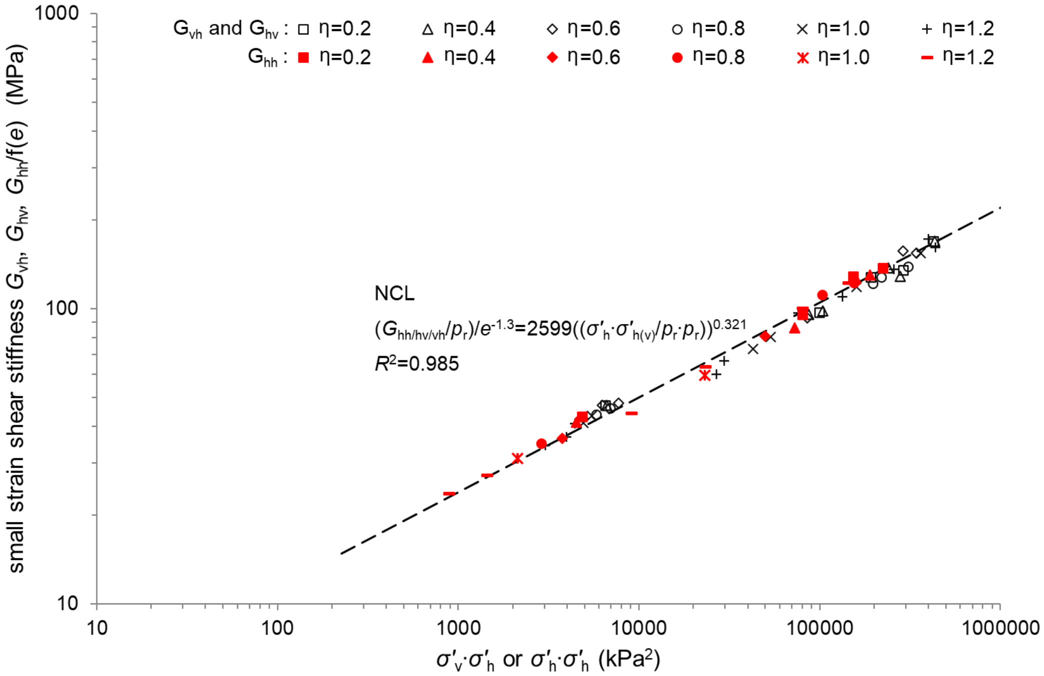

10(b)

Figure 10 Small strain shear stiffness of reconstituted specimens at different stress ratios (a) against the mean effective stress (b) against the product of effective principal stresses

Stage II-Anisotropy approaching the critical state

After reaching the value of 1.2, the stress ratio η shows little variation as the specimens approach the critical state, then the development of the anisotropy is mainly related to the large strains induced by shearing. The small strain stiffnesses of undisturbed specimens at different axial strain levels are plotted in figure 11. It can be observed in figure 11(a) that not only G_{hh}, but also G_{hv} and G_{vh} start to decrease as the strain increases. Compared to it before shearing, under the same p', G_{hh} is reduced by about 50% and $G_{hv/vh}$ is reduced by about 30% at the axial strain around 25%. The average value of stiffness ratio G_{hh}/G_{hv} is about 0.91 around the critical state, which is less than it at the end of first stage of 0.98, indicating that the undisturbed specimen again becomes anisotropic as sheared to critical state. When plotted against the product of principal stresses as shown in figure 11(b), all of G_{hh}, G_{hv} and G_{vh} start to decrease from the corresponding NCLs, indicating the occurrence of intact structure destruction, which is most likely caused by the large shear strains to reach the critical state. Around critical state, under the same stress product, G_{hh} is reduced by about 40% and $G_{hv/vh}$ is reduced by about 30%. After reaching an axial strain of 15%, G_{hv} and G_{vh} seem to become stable, and a possible critical state line (CSL) can be fitted, while G_{hh} still has a reducing trend, it may be stable with further strain development. This decreasing trend of small strain shear stiffness during shearing has also been reported for other soils (e.g. Kuribayashi et al., 1975; Goudarzy et al., 2018; Prashant et al., 2019; Zuo & Baudet, 2020). Based on DEM simulations, reasonable explanation has been reported that the coordination number at critical state becomes smaller compared to its initial value, and it is more significant on the horizontal plane (Gu et al., 2014, 2017). The more destruction on the horizontal plane makes G_{hh} decrease the most, and contributes to the anisotropy evolution during shearing.

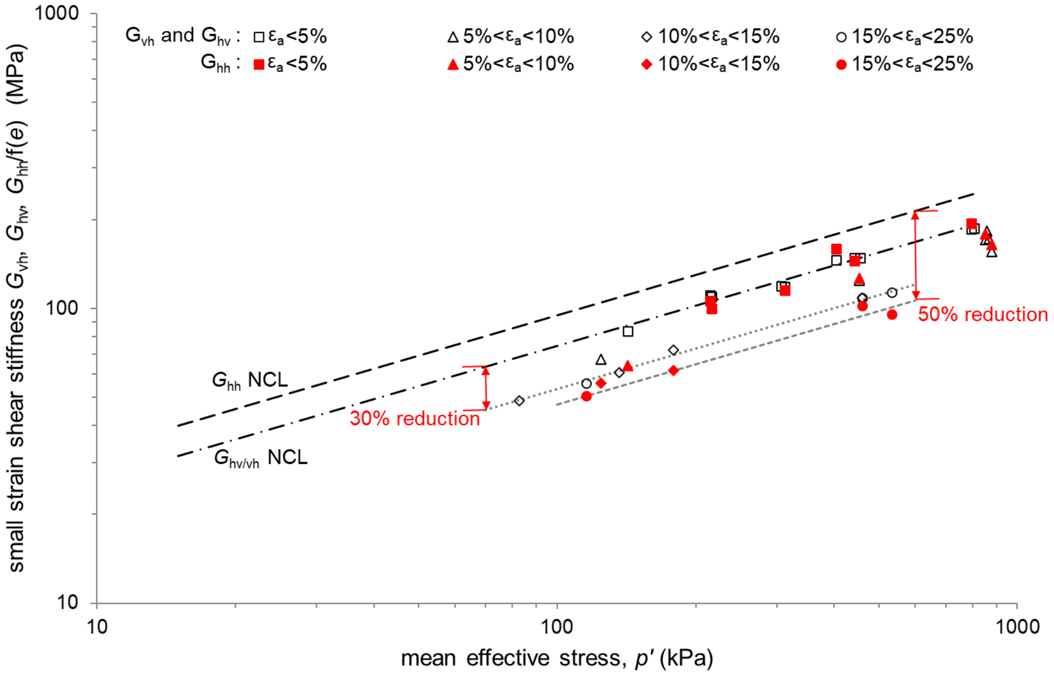

11(a)

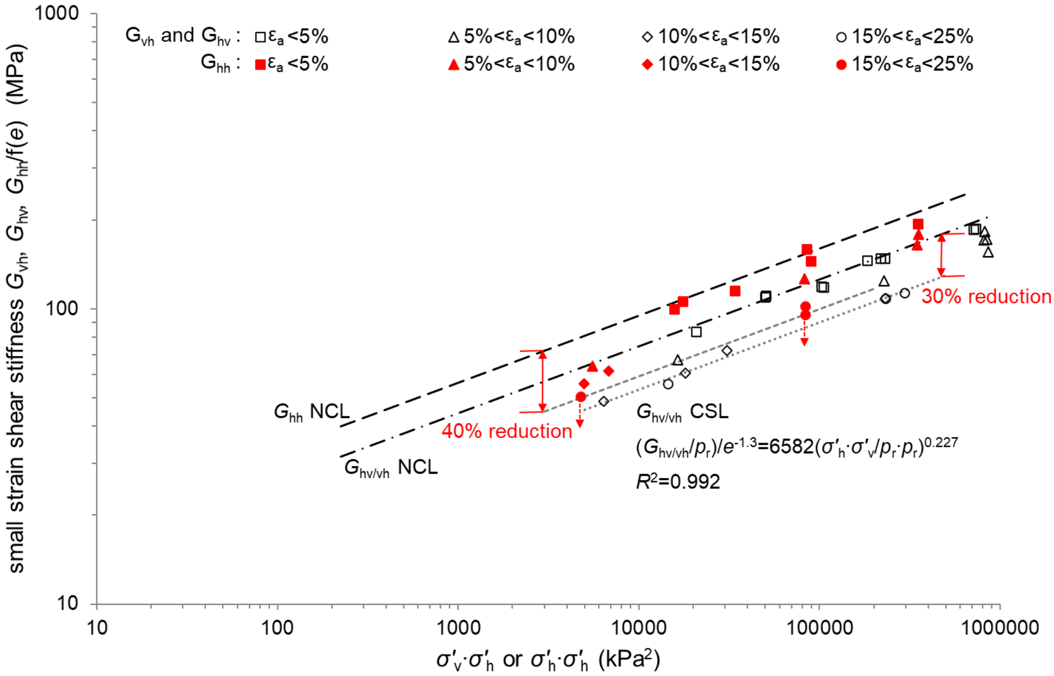

11(b)

Figure 11 Small strain shear stiffness of undisturbed specimens at different axial strains (stress ratio η around 1.2) (a) against the mean effective stress (b) against the product of effective principal stresses

The small strain stiffnesses of reconstituted specimens at different axial strain levels are plotted in figure 12. It shows that the reduction of stiffnesses during the strain development is not as significant as it for the undisturbed ones. Under the same *p'* as shown in figure 12(a), compared to the initial value, G_{hh} is reduced by about 44% and $G_{hv/vh}$ is reduced by about 23% at the axial strain around 25%. The average value of stiffness anisotropy ratio G_{hh}/G_{hv} is about 0.73 around the critical state, and is quite close to 0.75, which is the value at the end of first stage, indicating a unsignificant evolution of anisotropy during large strain development. While under the same stress product as shown in figure 12(b), both G_{hh} and $G_{hv/vh}$ start to decrease from the NCL and are reduced by about 20% around the critical state, again confirming a structure destruction, but not as significant as undisturbed specimens. A unique CSL can be fitted for all the stiffnesses, which means after destruction the soil structure still remains almost isotropic, and the anisotropy is mostly induced by the stress state. For reconstituted specimens, G_{hh} does not have more reduction than $G_{hv/vh}$ during shearing as what has been observed for undisturbed ones, a possible explanation could be that the bondings of particles or aggregates on the horizontal and vertical planes are already much weakened upon reconstitution, the influence of a little more destruction on the horizontal plane on G_{hh} is then not significant enough to be observed.

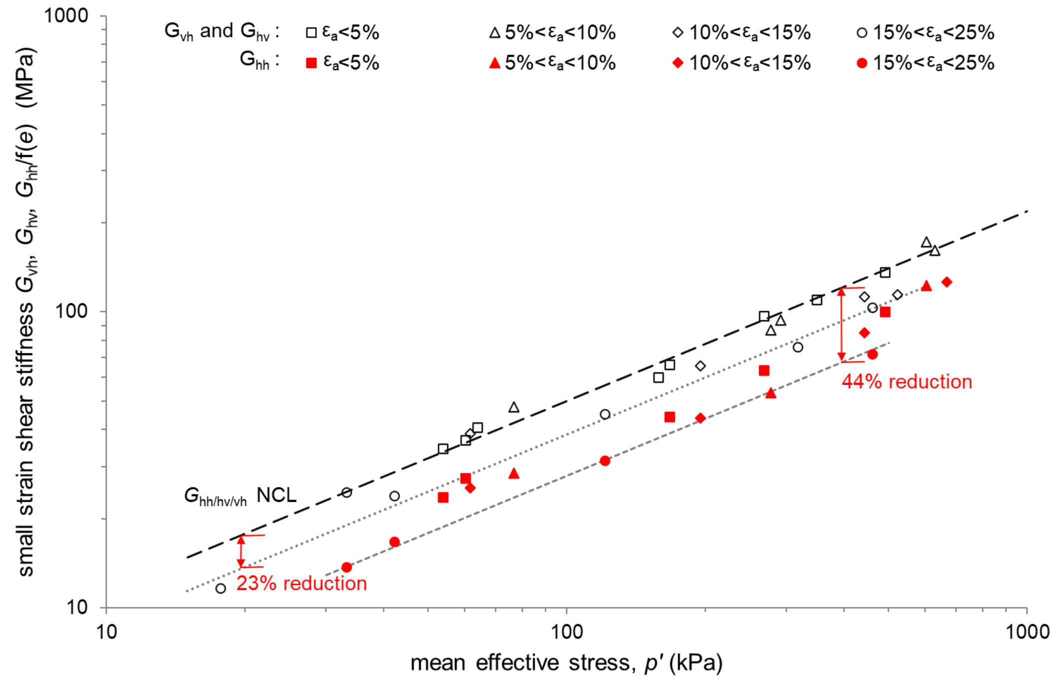

12(a)

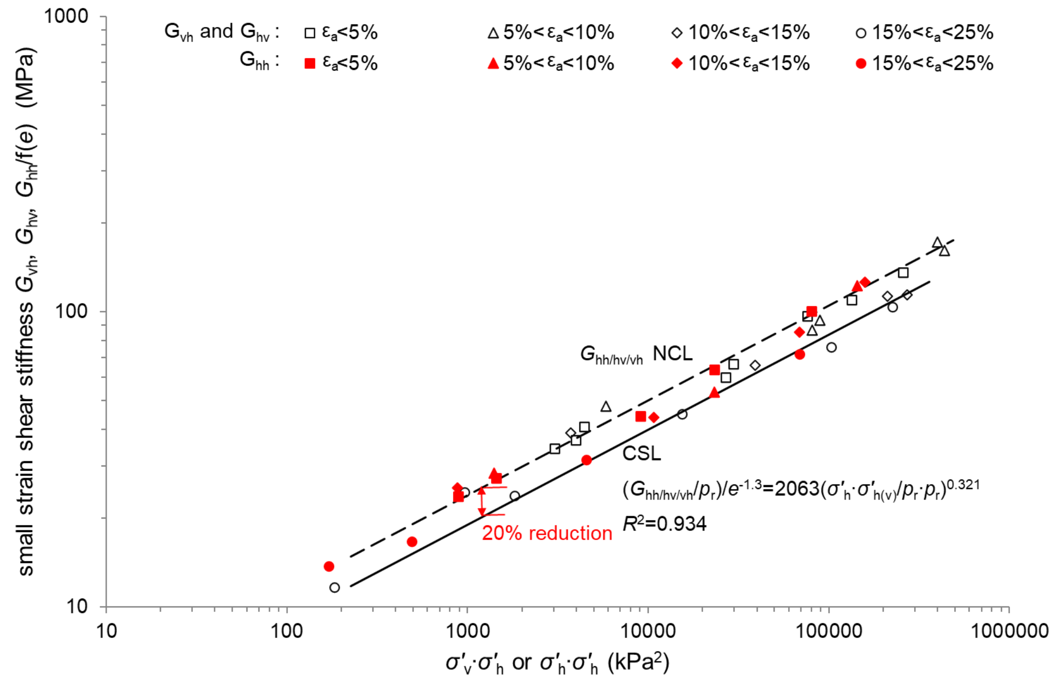

12(b)

Figure 12 Small strain shear stiffness of reconstituted specimens at different axial strains (stress ratio η around 1.2) (a) against the mean effective stress (b) against the product of effective principal stresses

The stiffness ratio G_{hh}/G_{hv} is then plotted against the effective principal stress ratio σ'_v/σ'_h to better demonstrate the evolution of stress-induced anisotropy during shearing for both undisturbed and reconstituted specimens. It can be seen in figure 13 that for undisturbed loess, G_{hh}/G_{hv} starts to decrease as σ'_v/σ'_h increases, and it turns from anisotropic to isotropic at σ'_v/σ'_h around 3.0 (corresponding to η of 1.2), indicating the effect of inherent structure anisotropy has been gradually cancelled by the increasing stress anisotropy. While as the shearing continues, the structure anisotropy starts to change since more soil structure destruction occurs on the horizontal plane due to the large deformation, G_{hh}/G_{hv} then keeps decreasing with σ'_v/σ'_h almost constant around 3.1 (corresponding to η of 1.25), and the specimen turns to be anisotropic again. For reconstituted loess, G_{hh}/G_{hv} decreases as σ'_v/σ'_h increases, and the specimen turns from isotropic to anisotropic gradually during shearing. It becomes stable at the critical state and there is no obvious influence of structure destruction observed. It then can be further inferred that when the effect of intact structure of undisturbed loess is further or even fully erased by continuous shearing, it tends to a similar anisotropy as the reconstituted loess at last.

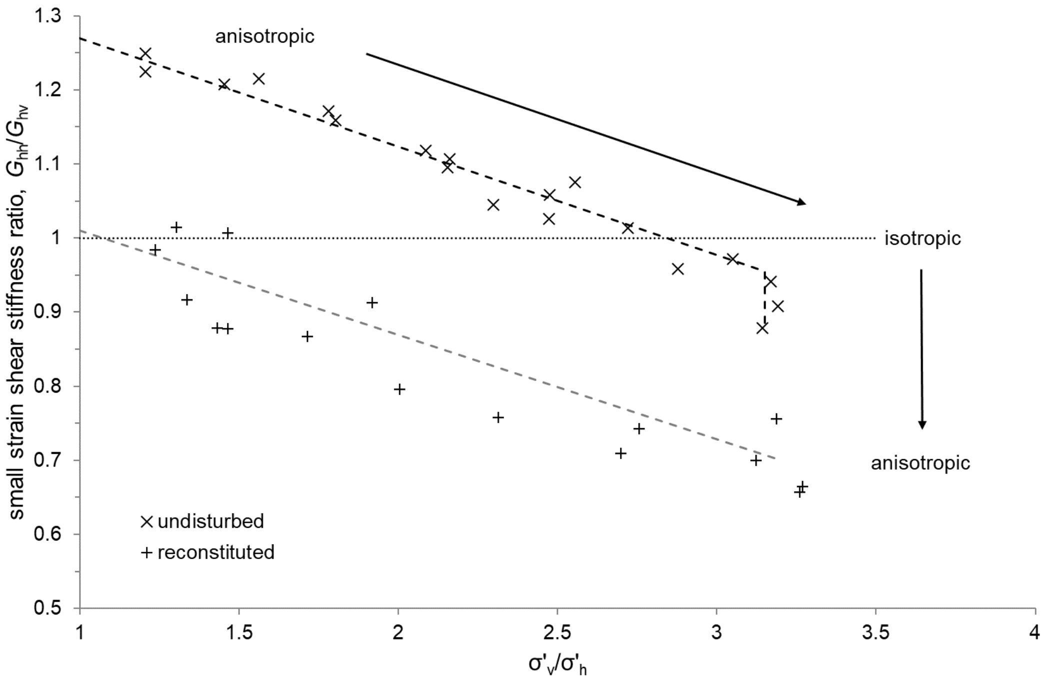

Figure 13 The development of stiffness anisotropy with the effective principal stress ratio

SEM observations

Figure 14 shows the horizontal and vertical planes of undisturbed specimen after shearing. Compared to the planes before shearing as shown in figure 7, it shows distinct soil structure damage and many more cracks can be clearly observed after shearing to critical state, especially on the horizontal plane. The aggregates are less coated and tend to break up into single particles, and the contacts between aggregates or particles are much less bonded and tend to break down. The large voids between aggregates are less observed, as a result of the occupation by the increasing detached particles, as well as the aggregates rearrangement caused by the large shear deformation. For reconstituted loess as shown in figure 15, the structure destruction is less significant. However, instead of aggregates, there are still more detached single silt or clay particles with less coated surfaces and less bonded contacts, indicating a further soil particle rearrangement due to the shearing to large deformation. For both undisturbed and reconstituted specimens, despite the damage to soil structure, the disintegration of aggregates and detachment of particles are also likely to be the evidence of the reduction in soil coordination number, which causes the decrease in the small strain stiffness at the critical state.

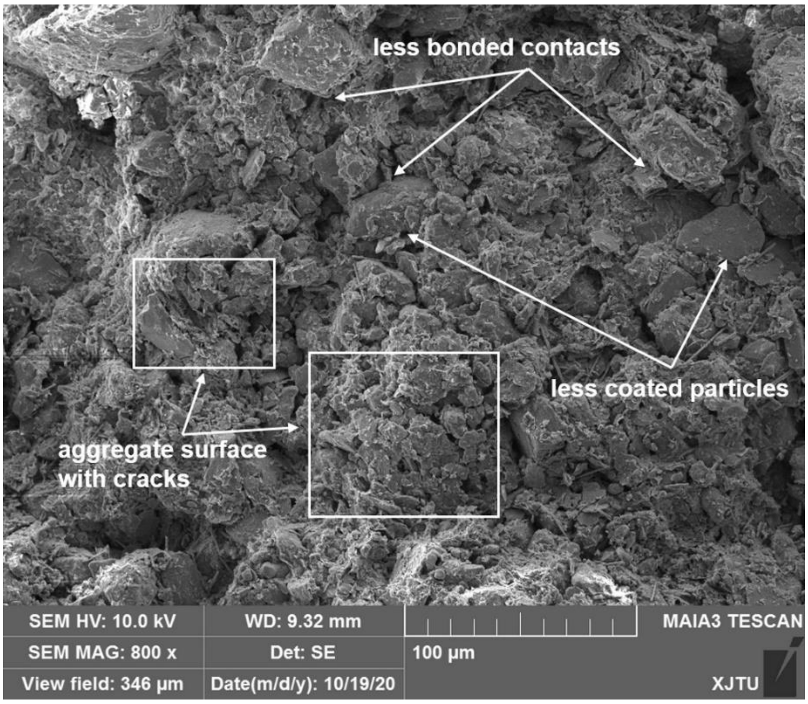

14(a)

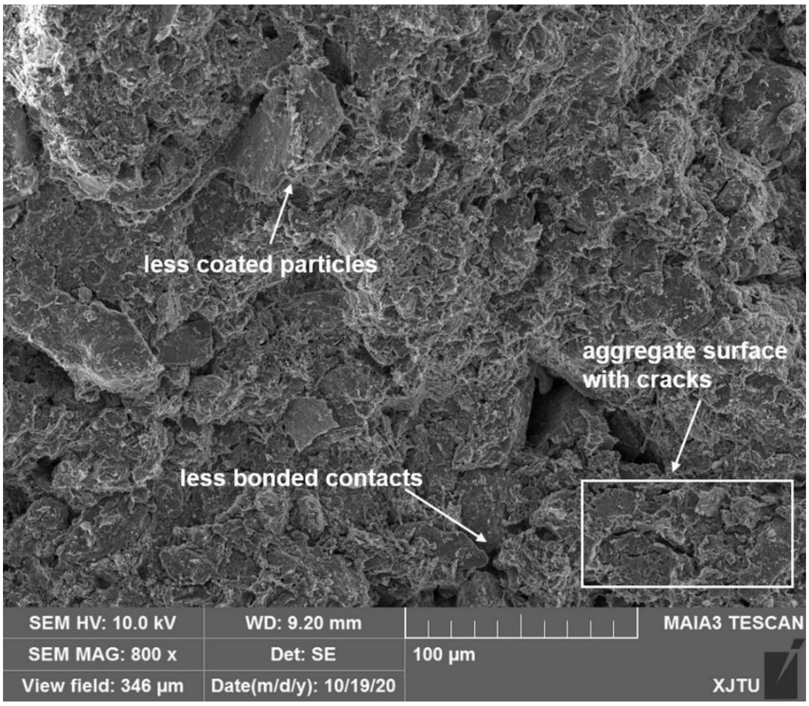

14(b)

Figure 14 SEM observations of undisturbed loess after shearing (a) horizontal plane (b) vertical plane

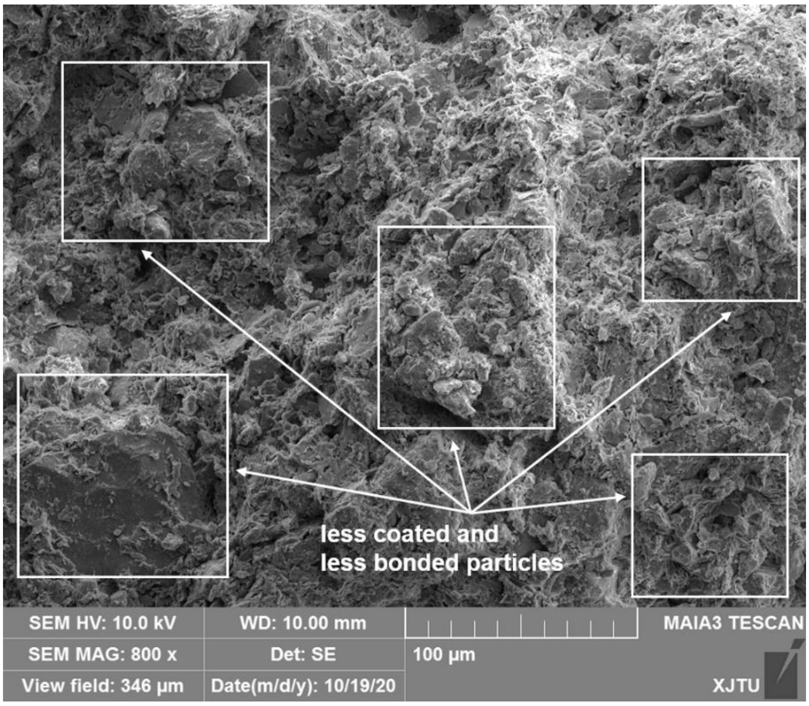

15(a)

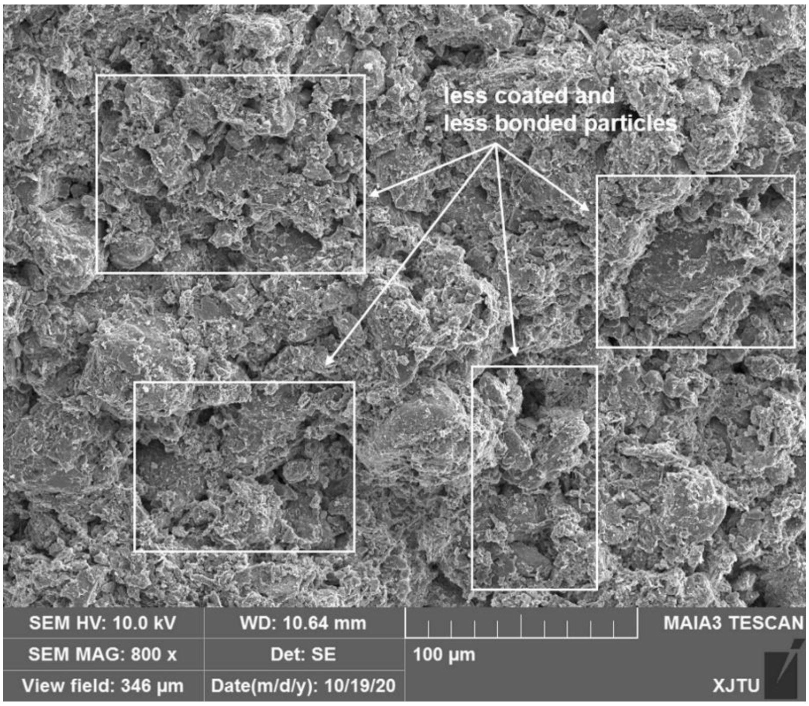

15(b)

Figure 15 SEM observations of reconstituted loess after shearing (a) horizontal plane (b) vertical plane

Conclusions

Both undisturbed and reconstituted specimens of a typical clayey loess were tested with bender elements and local LVDTs equipped triaxial apparatus to study the inherent and stress-induced small strain shear stiffness anisotropy. The results reveal the important influence of intact structure on the small strain stiffness anisotropy of loess soils.

Under isotropic stress state, a clear intact structure effect and the inherent anisotropy have been found for the undisturbed specimens, the average stiffness anisotropy ratio of G_{hh}/G_{hv} equals 1.27, and the average global strain increment ratio $\Delta\varepsilon_r/\Delta\varepsilon_a$ equals 1.98. This inherent anisotropy is also supported by micro-structure observations that an oriented aggregates arrangement with strong bondings has been revealed. The reconstituted specimens prepared with moist tamping method have much lower small strain shear stiffnesses and the average stiffness ratio G_{hh}/G_{hv} is 1.01, since the intact structure is destroyed and more isotropic and less stable structure is formed during specimen reconstitution.

During shearing, for undisturbed loess, G_{hh}/G_{hv} decreases as stress ratio η increases, the effect of inherent structure anisotropy has been gradually cancelled by the increasing stress anisotropy. After η becomes stable, as sheared to large strains the intact structure destruction occurs, then G_{hh}/G_{hv} decreases further and the specimen turns to be anisotropic again around the critical state. While for reconstituted loess, G_{hh}/G_{hv} decreases as stress ratio η increases, and the specimen turns from isotropic to anisotropic gradually as shearing continues. It becomes stable at the critical state and there is no obvious influence of structure destruction observed. It then can be further inferred that when the effect of intact structure of undisturbed loess is fully erased, it will tend toward the same anisotropy as the reconstituted loess at last.

Acknowledgement

The work was supported by the National Natural Science Foundation of China (Project No. 41772316), the Major Program of National Natural Science Foundation of China (Project No. 41790441), the National Key Research and Development Plan (Project No. 2018YFC1504701), the China Postdoctoral Science Foundation (Project No. 2019M663729) and the Youth Project of Natural Science Basic Research Plan in Shaanxi Province (Project No. 2020JQ-033).

Notations

NCL normal compression line

CSL critical state line

G_{vh}, G_{vh} small strain shear stiffness in vertical plane

G_{hh} small strain shear stiffness in horizontal plane

p_r reference stress taken as 1kPa

e void ratio

$f(e)$ function of void ratio

S_{vh}, S_{hh} soil small strain shear stiffness parameter

n_v, n_h soil small strain shear stiffness parameter

σ'_v effective principal stresses in vertical direction

σ'_h effective principal stresses in horizontal direction

p' mean effective stress

D_{50} mean particle size

q deviatoric stress

e_0 initial void ratio before shearing

p'_0 initial mean effective stress before shearing

ε_v volumetric strain

Δu excess pore water pressure

η stress ratio

v specific volume

ε_a axial strain

ε_r radial strain

$\Delta\varepsilon_a$ increment of axial strain

$\Delta\varepsilon_r$ increment of radial strain

$\Delta\varepsilon_s$ initial increment of shear strain

Δq initial increment of deviatoric stress

G_0 initial shear stiffness

References

Ackerley, S.K., Standing, J.R., Hosseini Kamal, R. (2016). A system for measuring radial local strains in triaxial apparatus. *Géotechnique* **66**, No. 6, 515-522.

Arthur, J.R.F. & Menzies, B.K. (1972). Inherent anisotropy in a sand. *Géotechnique* **22**, No. 1, 115-128.

Bellotti, R., Jamiolkowski, M., Lo Presti, D.C.F., O'Neill, D.A. (1996). Anisotropy of small strain stiffness in Ticino sand. *Géotechnique* **46**, No. 1, 115-131.

Bahadori, H., Ghalandarzadeh, A., Towhata, I. (2008). Effect of non plastic silt on the anisotropic behavior of sand. *Soils and Foundations* **48**, No. 4, 531-545.

Cai, Y., Dong, Q., Wang, J., Gu, C., Xu, C. (2015). Measurement of small strain shear modulus of clean and natural sands in saturated condition using bender element test. *Soil dynamics and Earthquake Engineering* **76**, 100-110.

Callisto, L. & Rampello, S. (2002) Shear strength and small-strain stiffness of a natural clay under general stress conditions. *Géotechnique* **52**, No. 8, 547-560.

Cascante, G. & Santamarina, J.C. (1996). Interparticle contact behaviour and wave propagation. *Journal of Geotechnical Engineering* **122**, No. 10, 831-839.

Cho, G.C., Dodds, J.S., Santamarina, J.C. (2006). Particle shape effects on packing density, stiffness, and strength: natural and crushed sands. *Journal of Geotechnical and Geoenvironmental Engineering*, *ASCE* **132**, No. 5, 591-602.

Cho, W. & Finno, R.J. (2010). Stress-strain responses of block samples of compressible Chicago glacial clays. *Journal of Geotechnical and Geoenvironmental Engineering*, *ASCE* **136**, No. 1, 178-188.

Choo, J., Jung, Y., Chung, C. (2011). Effect of directional stress history on anisotropy of initial stiffness of cohesive soils measured by bender element tests. *Soils and Foundations* **51**, No. 4, 737-747.

Ezaoui, A. & Di Benedetto, H. (2009). Experimental measurements of the global anisotropic elastic behaviour of dry Hostun sand during triaxial tests, and effect of sample preparation. *Géotechnique* **59**, No. 7, 621-635.

Fioravante, V. (2000). Anisotropy of small strain stiffness of Ticino and Kenya sands from seismic wave propagation measured in triaxial testing. *Soils and Foundations* **40**, No. 4, 129-142.

Gao, G. (1988). Formation and development of the structure of collapsing loess in China. *Engineering Geology* **25**, No. 2-4, 235-245.

Gasparre, A. & Coop, M.R. (2006). Techniques for performing small-strain probes in the triaxial apparatus. *Géotechnique* **56**, No. 7, 491-495.

Gasparre, A., Nishimura, S., Coop, M.R., Jardine, R.J. (2007a). The influence of structure on the behaviour of London Clay. *Géotechnique* **57**, No. 1, 19-31.

Gasparre, A., Nishimura, S., Minh, N.A., Coop, M.R., Jardine, R.J. (2007b). The stiffness of natural London Clay. *Géotechnique* **57**, No. 1, 33-47.

Ghadr, S. (2020). Effect of grain size on undrained anisotropic behaviour of sand-fibre composite. *Transportation Geotechnics* **22**, 100323.

Goudarzy, M., König, D. & Schanz, T. (2018). Interpretation of small and intermediate strain characteristics of Hostun sand for various stress states. *Soils and Foundations* **58**, No. 6, 1526-1537.

Gu, X., Huang, M. & Qian, J. (2014). DEM investigation on the evolution of microstructure in granular soils under shearing. *Granular Matter* **16**, No. 1, 91–106.

Gu, X., Hu, J. & Huang, M. (2017). Anisotropy of elasticity and fabric of granular soils. *Granular Matter* **19**, 33.

Hardin, B.O. & Richart, F.E. (1963). Elastic wave velocities in granular soils. *Journal of the Soil Mechanics and Foundations Division*, *ASCE* **89**, SM1, 39-56.

Heitor, A., Indraratna, B., Rujikiatkamjorn, C. (2013). Laboratory study of small-strain behavior of a compacted silty sand. *Canadian Geotechnical Journal*

50, No. 2, 179-188.

Heller, F. & Liu, T.S. (1982). Magnetostratigraphical dating of loess deposits in China. *Nature* **300**, 431-433.

Ignat, R., Baker, S., Holmén, M., Larsson, S. (2019). Triaxial extension and tension tests on lime-cement-improved clay. *Soils and Foundations* **59**, No. 5, 1399-1416.

Jamiolkowski, M., Lancellotta, R., Lo Presti, D.C.F. (1995). Remarks on the stiffness at small strain of six Italian clays. In *Pre-failure deformation characteristics of geomaterials* (eds Shibuya, Mitachi and Miura), Vol. 2, pp. 817-836. Rotterdam, the Netherland: A.A. Balkema.

Jiang, G., Tatsuoka, F., Flora, A., Koseki, J. (1997). Inherent and stress-state-induced anisotropy in very small strain stiffness of a sandy gravel. *Géotechnique* **47**, No. 3, 509-521.

Jiang, M., Zhang, F., Hu, H., Cui, Y., Peng, J. (2014). Structural characterization of natural loess and remolded loess under triaxial tests. *Engineering Geology* **181**, 249-260.

Jovičić, V., Coop, M.R., Simić, M. (1996). Objective criteria for determining G_{max} from bender element tests. *Géotechnique* **46**, No. 2, 357-362.

Jovičić, V. & Coop, M.R. (1997). Stiffness of coarse-grained soils at small strains. *Géotechnique* **47**, No. 3, 545-561.

Jovičić, V. & Coop, M.R. (1998). The measurement of stiffness anisotropy in clays with bender element tests in the triaxial apparatus. *Geotechnical Testing Journal* **21**, No. 1, 3–10.

Kim, T. & Finno, R.J. (2012). Anisotropy evolution and irrecoverable deformation in triaxial stress probes. *Journal of Geotechnical and Geoenvironmental Engineering*, *ASCE* **138**, No. 2, 155-165.

Kuribayashi, E., Iwasaki, T., Tatsuoka, F. (1975) Effects of stress-strain conditions on dynamic properties of sands. *Proceedings of the Japan Society of Civil Engineers* **1975**, No. 242, 105-114.

Kuwano, R., Connolly, T. M. & Kuwano, J. (1999). Shear stiffness anisotropy measured by multi-directional bender element transducers. In *Pre-failure deformation characteristics of geomaterials* (eds M. Jamiolkowski, R. Lancellota and D. Lo Presti), vol. 1, pp. 205–212. Rotterdam, the Netherlands: A. A. Balkema.

Liu, T. (1985). Loess and Environment. China Ocean Press, Beijing.

Lee, J.S., Dodds, J., Santamarina, J.C. (2007). Behaviour of rigid-soft particle mixtures. *Journal of Materials in Civil Engineering*, *ASCE* **19**, No. 2, 179-184.

Leong, E.C., Yeo, S.H., Rahardjo, H. (2005) Measuring shear wave velocity using bender elements. *Geotechnical Testing Journal, ASTM* **28**, No.5, 488–498.

Li, P., Vanapalli, S.K., Li, T. (2016). Review of collapse triggering mechanism of collapsible soils due to wetting. *Journal of Rock Mechanics and Geotechnical Engineering* **8**, No. 2, 256-274.

Li, Q., Ng, C.W.W., Liu, G.B. (2012). Determination of small-strain stiffness of Shanghai clay on prismatic soil specimen. *Canadian Geotechnical Journal* **49**, No. 8, 986-993.

Li, W. & Coop, M.R. (2019). Mechanical behaviour of Panzhihua iron tailings. *Canadian Geotechnical Journal* **56**, No. 3, 420-435.

Liang, Q., Li, J., Wu, X., Zhou, A. (2015). Anisotropy of Q_2 loess in the Baijiapo Tunnel on the Lanyu Railway, China. *Bulletin of Engineering Geology and the Environment* **75**, No. 1, 109-124.

Liu, X., Zhang, N., Lan, H. (2019). Effects of sand and water contents on the small-strain shear modulus of loess. *Engineering Geology* **260**, 105202.

Mašín, D. & Rott, J. (2014). Small strain stiffness anisotropy of natural sedimentary clays: review and a model. *Acta Geotechnica* **9**, No. 2, 299-312.

Mitaritonna, G., Amorosi, A., Cotecchia, F. (2014). Experimental investigation of the evolution of elastic stiffness anisotropy in a clayey soil. *Géotechnique* **64**, No. 6, 463-475.

Ng, C.W.W. & Yung, S.Y. (2008). Determination of the anisotropic shear stiffness of an unsaturated decomposed soil. *Géotechnique* **58**, No. 1, 23-35.

Ng, C.W.W., Mu, Q.Y., Zhou, C. (2017a). Effects of soil structure on the shear behaviour of an unsaturated loess at different suctions and temperatures. *Canadian Geotechnical Journal* **54**, No. 2, 270-279.

Ng, C.W.W., Kaewsong, R., Zhou, C., Alonso, E.E. (2017b). Small strain shear moduli of unsaturated natural and compacted loess. *Géotechnique* **67**, No. 7, 646-651.

Pennington, D.S., Nash, D.F.T., Lings, M.L. (1997). Anisotropy of G_0 shear stiffness in Gault Clay. *Géotechnique* **47**, No. 3, 391-398.

Pennington, D.S., Nash, D.F.T, Lings, M.L. (2001) Horizontally-mounted bender elements for measuring anisotropic shear moduli in triaxial clay specimens. *Geotechnical Testing Journal, ASTM* **24**, No.2, 133–144.

Prashant, A., Bhattacharya., D. & Gundlapalli, S. (2019). Stress-state dependency of small-strain shear modulus in silty sand and sandy silt of Ganga. *Géotechnique* **69**, No. 1, 42-56.

Rampello, S., Viggiani, G.M.B., Amorosi, A. (1997). Small-strain stiffness of reconstituted clay compressed along constant triaxial effective stress ratio paths. *Géotechnique* **47**, No. 3, 475-489.

Santagata, M., Germaine, J.T., Ladd, C.C. (2005). Factors affecting the initial stiffness of cohesive soils. *Journal of Geotechnical and Geoenvironmental Engineering, ASCE* **131**, No. 4, 430-441.

Song, B., Tsinaris, A., Anastasiadis, A., Pitilakis, K., Chen, W. (2017). Small-strain stiffness and damping of Lanzhou loess. *Soil dynamics and Earthquake Engineering* **95**, 96-105.

Teachavorasinskun, S. & Lukkanaprasit, P. (2008). Stress induced and inherent anisotropy on elastic stiffness of soft clays. *Soils and Foundations* **48**, No. 1, 127-132.

Viana da Fonseca, A. Ferreira, C., Fahey, M. (2009). A framework interpreting bender element tests, combining time-domain and frequency-domain methods. *Geotechnical Testing Journal, ASTM* **32**, No. 2, 91-107.

Viggiani, G. & Atkinson, J.H. (1995a). Interpretation of bender element tests.

Géotechnique **45**, No. 1, 149-154.

Viggiani, G. & Atkinson, J.H. (1995b). Stiffness of fine-grained soil at very small strains. *Géotechnique* **45**, No. 2, 249-265.

Wang, Y.H. & Mok, C.M.B. (2008) Mechanisms of small-strain shear-modulus anisotropy in soils. *Journal of Geotechnical and Geoenvironmental Engineering, ASCE* **134**, No. 10, 1516-1530.

Xu, L. & Coop, M.R. (2016). Influence of structure on the behaviour of a saturated clayey loess. *Canadian Geotechnical Journal* **53**, No. 6, 1026-1037.

Xu, L., Gao, C., Wei, X. (2019). Anisotropic behavior of a saturated clayey loess. *Géotechnique Letters* **9**, No. 1, 28-34.

Yang, J. & Liu, X. (2016). Shear wave velocity and stiffness of sand: the role of non-plastic fines. *Géotechnique* **66**, No. 6, 500-514.

Yimsiri, S. & Soga, K. (2011). Cross-anisotropic elastic parameters of two natural stiff clays. *Géotechnique* **61**, No. 9, 809-814.

Zuo, L. & Baudet, B.A. (2020). Normalised behaviour of a non-plastic silt–pumice sand mixture. *Géotechnique* **70**, No. 9, 822-832.

Zuo, L., Xu, L., Baudet, B.A., Gao, C., Huang, C. (2020) The structure degradation of a silty loess induced by long-term water seepage. *Engineering Geology* **272**, 105634.

List of figures

Figure 1 Schematic diagram triaxial apparatus equipped with vertical and horizontal bender elements and axial and radial LVDTs

Figure 2 Typical results (a) CSLs and shear paths in v-lnp' plane (b) shearing stress-strain curves (c) effective stress ratio vs. volumetric strain in drained tests (d) effective stress ratio vs. excess pore water pressure in undrained tests (d) CSLs and shear paths in v-lnp' plane (e) compression and shearing stress paths and stress ratios where small strain shear stiffness measured

Figure 3 Isotropic compression curves of undisturbed and reconstituted specimens

Figure 4 Strain increment ratio of undisturbed and reconstituted specimens during isotropic compression

Figure 5 Small strain shear stiffness for undisturbed specimens under isotropic stress condition (a) stiffness in vertical and horizontal planes (b) stiffness ratios

Figure 6 Small strain shear stiffness for reconstituted specimens under isotropic stress condition (a) stiffness in vertical and horizontal planes (b) stiffness ratios

Figure 7 SEM observations of undisturbed loess before compression (a) horizontal plane (b) vertical plane

Figure 8 SEM observations of reconstituted loess before compression (a) horizontal plane (b) vertical plane

Figure 9 Small strain shear stiffness of undisturbed specimens at different stress ratios (a) against the mean effective stress (b) against the product of effective principal stresses

Figure 10 Small strain shear stiffness of reconstituted specimens at different stress ratios (a) against the mean effective stress (b) against the product of effective principal stresses

Figure 11 Small strain shear stiffness of undisturbed specimens at different axial strains (stress ratio η around 1.2) (a) against the mean effective stress (b) against the product of effective principal stresses

Figure 12 Small strain shear stiffness of reconstituted specimens at different axial strains (stress ratio η around 1.2) (a) against the mean effective stress (b) against the product of effective principal stresses

Figure 13 The development of stiffness anisotropy with the effective principal stress ratio

Figure 14 SEM observations of undisturbed loess after shearing (a) horizontal plane (b) vertical plane

Figure 15 SEM observations of reconstituted loess after shearing (a) horizontal plane (b) vertical plane